

1 **ANISOTROPY OF MASS TRANSFER DURING SINTERING OF**
2 **POWDER MATERIALS WITH PORE-PARTICLE STRUCTURE**
3 **ORIENTATION**

4
5
6 E. Torresani^a, D. Giuntini^b, C. Zhuc, T. Harrington^c,
7 K. S. Vecchio^c, A. Molinarid, R. K. Bordia^e, E.A. Olevsky^{a,c,1}
8

9 ^a San Diego State University, 5500 Campanile Drive, CA 92182

10 ^b Hamburg University of Technology, Denickestrasse 15, 21073, Hamburg, Germany

11 ^c University of California, San Diego, 9500 Gilman Drive, La Jolla, CA 92093, USA

12 ^d University of Trento, Via Sommarive 9, 38123 Trento, Italy

13 ^e Clemson University, 161 Surrine Hall, Clemson, SC 29634, USA
14
15

16 **Abstract:**
17

18 A micromechanical model for the shrinkage anisotropy during sintering of metallic
19 powders is proposed and experimentally assessed. The framework developed for
20 modeling sintering based on the mechanism of grain boundary diffusion is extended to
21 take into account the dislocation pipe-enhanced volume diffusion. The studied iron
22 powder samples are pre-shaped into their green forms by uniaxial cold pressing before
23 sintering step. The resultant green bodies are anisotropic porous structures, with
24 inhomogeneous plastic deformation at the inter-particle contacts. These non-uniformities
25 are considered to be the cause of the anisotropic dislocation pipe diffusion mechanisms,
26 and thus of the undesired shape distortion during shrinkage. The proposed model
27 describes the shrinkage rates in the compaction loading and transverse directions, as
28 functions of both structural and geometric activities of the samples. Dislocation densities
29 can be estimated from such equations using dilatometry and image analysis data. The
30 reliability and applicability of the developed modeling framework is verified by comparing
31 the calculated dislocation densities with outcomes of nanoindentation and electron
32 backscatter diffraction derived lattice rotations.
33

34 **Keywords:** Sintering; Anisotropy; Volume diffusion; Dislocation density;
35 Nanoindentation; Electron Backscatter Diffraction.
36

37 **1. Introduction**

38 In the conventional press-and-sinter process of powder metallurgy, green parts obtained
39 by cold compaction are sintered to form dense bulk parts via the metallic bonding between
40 the powder particles. This occurs through the formation and growth of the so-called necks,
41 promoted by mass transport phenomena towards the inter-particle contact region. When
42 the source of atoms flowing towards the neck region lies within the bulk of the particles,
43 sintering is accomplished by shrinkage, leading to an overall dimensional change of the
44 parts [1]. The prediction of such a dimensional change is of great importance, since one
45 of the key attributes of powder metallurgy is net shape sintering of complex parts with
46 excellent dimensional precision, without any need of machining.

47 In the literature, various approaches are used to investigate sintering at different scales.
48 The microscale approach is based on the classical theory of sintering that describes the
49 growth of the sintering necks as a function of temperature and time, due to the driving
50 force linked to the free surface area of the powders and to the occurrence of various mass
51 transport mechanisms. Shrinkage kinetics laws are proposed for each mass transport
52 mechanism, based on the assumption that powder particles are rigid spheres in a point
53 contact at the beginning of the sintering process [2–16]. The effect of the initial cold
54 compaction is therefore mostly neglected. The macroscale approach is utilized in most
55 modern studies, where the behavior of the porous body during sintering is described using
56 continuum mechanics [17–26]. This approach is similar to the theories of plasticity of
57 porous bodies [27–36] employed for modeling of powder pressing. It investigates the
58 dimensional changes of porous bodies as a consequence of the flow of material from the
59 solid matrix containing pores, and treats sintering as a rheological phenomenon [37,38].

60

61 Solid state sintering is a thermally activated process, where the contributions from several
62 mass transport mechanisms, such as surface, grain boundary, and lattice diffusion, are
63 responsible for neck growth and powder consolidation. Surface diffusion is mostly
64 accountable for neck growth and the consequent material strengthening [13,39–41].
65 Different works [42-44] show, in the case of sinter-forging and constrained sintering, that
66 the sintering shrinkage of powders can be anisotropic, due to the sintering conditions.
67 Otherwise in the case of free sintering it has been demonstrated that the anisotropic
68 shrinkage is a consequence of the anisotropic plastic deformation of the particles
69 promoted by uniaxial cold compaction [45]. Zavaliangos *et al.* [46,47] have considered
70 anisotropy to be a consequence of the different flattening and arrangement of particle-
71 particle contacts, the density of pores present on the grain boundaries, and oxide
72 fragmentation. In a previous work, Molinari *et al.* [48] proposed that anisotropy is due to
73 the effect of the structural defect densities introduced by cold compaction on bulk
74 diffusivity. This hypothesis was further developed by some of the authors of the present
75 paper; with studies on the kinetics of the diffusion mechanisms [48,49], microstructural
76 analysis on the deformed powder particles after cold compaction [50,51], and an initial
77 investigation on the effect of defects on diffusion [52]. One result indicated that shrinkage
78 kinetics are influenced by the dislocations formed in the powder particles during cold
79 compaction (structural activity). Namely, the inhomogeneous dislocation density
80 distribution inside the particles leads to anisotropic shrinkage kinetics, characterized by
81 greater densification parallel to the compaction direction (longitudinal) than perpendicular
82 to the compaction direction (transverse).

83 Grain boundary diffusion is generally considered to be the principal mass transfer
84 mechanism in solid state sintering [40,44,46,47]. However, taking into account the large
85 strains present within the particles of the initial green compact and the effect of
86 dislocations on diffusivity, especially during the early stages of sintering, volume diffusion
87 can be of greater importance. The effect of dislocations on bulk diffusivity is displayed
88 through the dislocation pipe diffusion model, according to which, bulk diffusivity is
89 proportional to the dislocation density, as reported by Hart [54,55]. Based on Hart's
90 equation for dislocation pipe diffusion and the equations of the classical theory of
91 sintering, Molinari *et al.* [49] estimated the dislocation density in the inter-particle contact
92 regions, obtaining quite high values, comparable to those typical of heavily cold worked
93 metals. However, the classic theories of sintering, as mentioned above, do not consider
94 the actual geometry of the contact regions, which is different than a single point, and
95 occupies an area that changes depending on the contact direction. These geometric
96 aspects can be analyzed and quantified in the metallographic sections using image
97 analysis software. Specifically, for the measurement of the contact lengths, a general
98 method, including a preliminary correction factor due to "distortion" and measurement
99 imprecisions, was demonstrated in previous studies [50,51]. Such microstructural
100 features of the green parts may further contribute to the anisotropic dimensional change
101 (geometric activity), since atoms flowing towards the neck surface originate in the inter-
102 particle regions. Other authors investigated the influence of shape and orientation of
103 particles and pores on shrinkage [56–59].

104 In the present work, the continuum theory of sintering is used to develop a
105 micromechanical model of the anisotropic dimensional change, inclusive of both the

106 contributions of structural and geometric activities, namely presence of dislocations and
107 of the flattened porous material morphology. The model proposed by Olevsky *et al.* [44]
108 is adapted to this case, in which volume diffusion is the principal mass transport
109 mechanism. This model is applied to the sintering of pure iron. Such a material choice
110 was made in order to rule out potential complications arising from the presence of
111 additional alloying elements altering the diffusivity of the powder compact, and to rely on
112 the wide availability of physical and chemical data on pure iron in the literature. The
113 dislocation densities along the different directions are calculated by plugging the
114 experimental data on the isothermal shrinkage of the sample at the different sintering
115 temperatures into the derived equations. The validity of the model is then assessed by
116 experimentally estimating dislocation densities with two different methods. The first
117 method is based on the correlation between dislocation densities and hardness measured
118 via nanoindentation, as proposed by Nix and Gao [61–63]. The second method relies on
119 EBSD lattice curvature data [64–66]. The comparison between calculated and measured
120 dislocation density values is accompanied by a parameter sensitivity study, and the
121 reliability of the model is discussed.

122

123 **2. Model Formulation**

124 The proposed micromechanical model is the adaptation of the work of Olevsky *et al.* [44]
125 to the volume diffusion case. In the earlier work by Olevsky *et al.*, it was assumed that the
126 main mass transfer mechanism was grain boundary diffusion, and diffusion was related
127 to micromechanical considerations through the chemical potential, according to Johnson

128 [11]. In the present case, the induced plastic deformation activates dislocation pipe
129 diffusion mechanisms, and therefore leads to noticeably enhanced volume diffusivity [52].
130 Therefore, for the study domain definition, the 2-D geometry employed in Olevsky *et al.*
131 [44] is extended to the 3-D case. The porous structure of the material can be schematized
132 with an assembly of simple-packed, oriented, prismatic particles, with ellipsoidal pores at
133 the junctions between them, as depicted in Fig. 1(a).

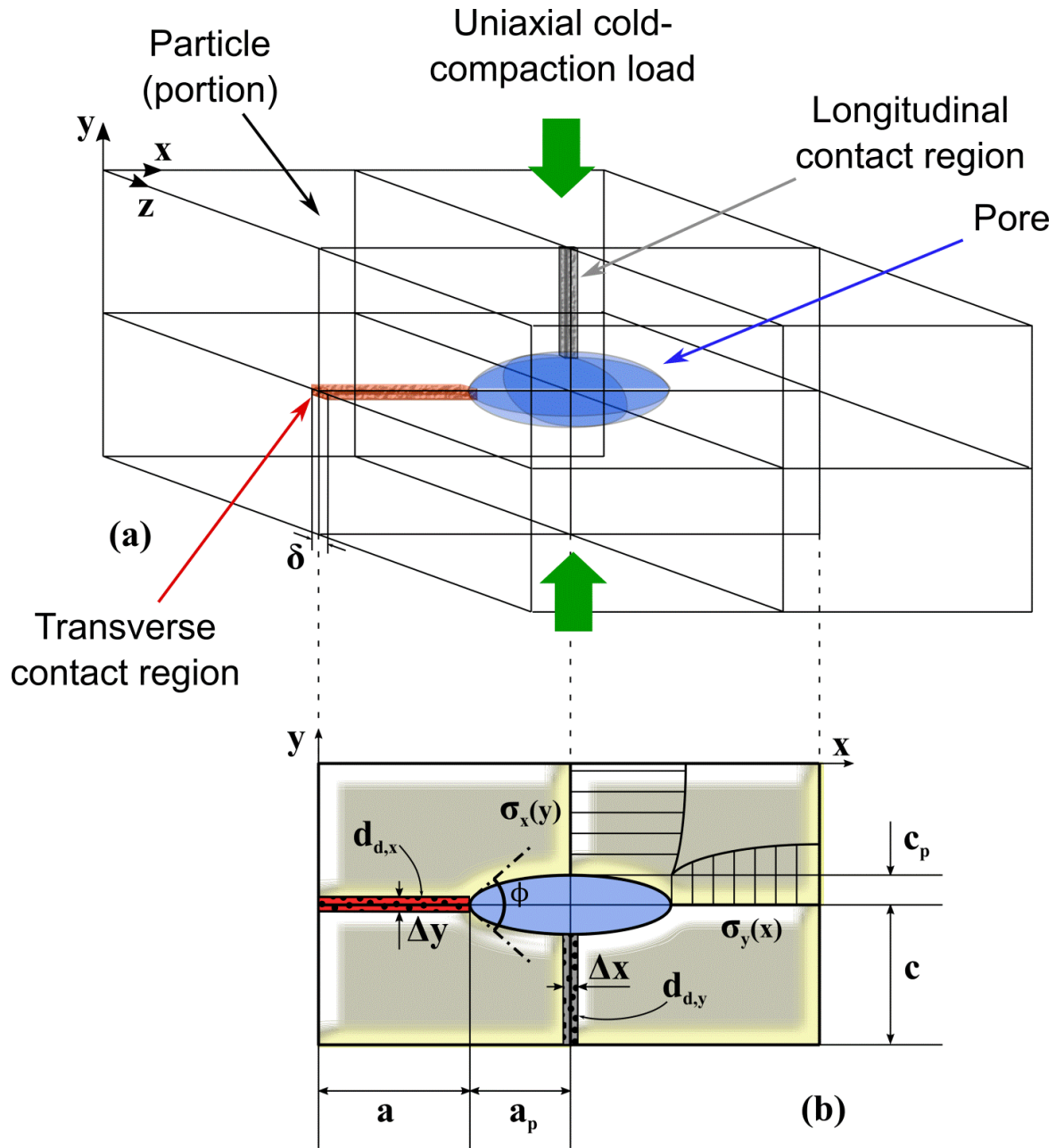


Fig. 1. Schematics of the study domain representative of the porous material's structure: (a) 3-D representation, where δ is the inter-particle boundary thickness; (b) 2-D view with micromechanics parameters designation.

134 A representative unit cell for the micromechanical study definition is chosen to be a cluster
 135 of eight particles with a central lenticular pore. Note that, due to the symmetry of the
 136 structure, it is sufficient to only take into consideration 1/8 of each particle, accordingly to
 137 the representation given in Fig. 1(a). The prismatic shape is a good approximation for

138 powder particles that have been flattened by cold compaction and allows a simple
 139 definition of all the geometric parameters that influence the shrinkage kinetics. As
 140 depicted in Fig. 1(a), the y-axis is defined oriented along the pre-sintering cold compaction
 141 direction (longitudinal direction), and thus x and z are defined as transverse directions.
 142 The notations, a , b and c define the semi-contact of the particles along x, z and y,
 143 respectively, and a_p , b_p and c_p the semi-axes of the pores in the same directions. In this
 144 coordinate system, the geometric features along the x and z direction are equivalent ($a =$
 145 b , $a_p = b_p$), and the semi-axes and contact along x and z are greater than the those along
 146 y ($a > c$, $a_p > c_p$). This geometry represents transversely isotropic symmetry [45].

147 The radii of curvature r_a , r_b and r_c for the ellipsoidal pores are thus defined as:

$$148 \quad r_a = r_b = \frac{c_p^2}{a_p}; \quad r_c = \frac{a_p^2}{c_p} \quad (1)$$

149 and the surface area of the pore is given by:

$$150 \quad S_p \approx 2\pi \left(\frac{a_p^2 + c_p^2 \frac{\tanh^{-1} \left(\sin \left(\cos^{-1} \left(\frac{c_p}{a_p} \right) \right) \right)}{\sin \left(\cos^{-1} \left(\frac{c_p}{a_p} \right) \right)}}{\sin \left(\cos^{-1} \left(\frac{c_p}{a_p} \right) \right)} \right) \quad (2)$$

151 As a result of this equivalence along the two transverse directions, the model is hereby
 152 developed in the reference system defined by the axes x and y, as shown in Fig. 1(b).

153 According to Johnson [11], at the inter-particle boundaries, the following normal stress
 154 distributions exist:

$$155 \quad \begin{cases} \sigma_x = b_{1x} \cdot y^2 + b_{2x} \cdot y + b_{3x} \\ \sigma_y = b_{1y} \cdot x^2 + b_{2y} \cdot x + b_{3y} \end{cases} \quad (3)$$

156 Due to the geometry of the study domain, the boundary conditions that these should
 157 satisfy for the x direction are:

$$158 \quad \begin{cases} \int_0^c \sigma_x dx = -\gamma_{sv} \cdot \sin\left(\frac{\phi}{2}\right) \\ \sigma_x(c) = \gamma_{sv} / r_c \\ \nabla \sigma_x(0) = \frac{\partial \sigma_x}{\partial y}(y=0) = 0 \end{cases} \quad (4)$$

159 where γ_{sv} (N/m) is the surface energy and ϕ is the dihedral angle. The dihedral angle is
 160 related to surface and grain boundary energy γ_{ss} (N/m), as follows:

$$161 \quad \gamma_{ss} = 2 \cdot \gamma_{sv} \cos\left(\frac{\phi}{2}\right) \quad (5)$$

162 The three Equations (4) represent: the balance of the forces acting at inter-particle
 163 junctions with the free surface tension of the pore, the normal stress in correspondence
 164 of the pore surface ($y = c$), and the symmetry of the stress distribution.

165 With these boundary conditions the values of the coefficients b_{1x} , b_{2x} and b_{3x} (3) are
 166 obtained:

$$167 \quad \begin{cases} b_{1x} = 3\gamma_{sv}/2 \left[\frac{1}{c^2 \cdot r_c} - \frac{1}{c^3} \cdot \sin\left(\frac{\phi}{2}\right) \right] \\ b_{2x} = 0 \\ b_{3x} = \gamma_{sv} \left[\frac{3}{2 \cdot c} \cdot \sin\left(\frac{\phi}{2}\right) - \frac{1}{2 \cdot r_c} \right] \end{cases} \quad (6)$$

168 Thus, the normal stress distribution along the transverse direction becomes:

$$169 \quad \sigma_x = 3\gamma_{sv}/2 \left\{ \frac{1}{c^2} \left[\frac{1}{r_c} - \frac{1}{c} \cdot \sin\left(\frac{\phi}{2}\right) \right] \cdot y^2 + \left[\frac{1}{c} \cdot \sin\left(\frac{\phi}{2}\right) - \frac{1}{3 \cdot r_c} \right] \right\} \quad (7)$$

170 An analogous procedure can be applied in the longitudinal direction to obtain:

171
$$\sigma_x = 3\gamma_{sv}/2 \left\{ \frac{1}{a^2} \left[\frac{1}{r_a} - \frac{1}{a} \cdot \sin\left(\frac{\phi}{2}\right) \right] \cdot x^2 + \left[\frac{1}{a} \cdot \sin\left(\frac{\phi}{2}\right) - \frac{1}{3 \cdot r_a} \right] \right\} \quad (8)$$

172 As anticipated, volume diffusion enhanced by dislocation activity is considered as the
 173 prevailing mass transport mechanism. Accordingly, the fluxes of matter in the x and y
 174 directions (J_x^V and J_y^V , mol·m⁻²·s⁻¹) are proportional to the chemical potential gradient,
 175 given by:

176
$$\begin{cases} J_x^V = -D_{eff,x}^V / (k \cdot T \cdot \Omega) \cdot \frac{\partial \mu}{\partial x} \\ J_y^V = -D_{eff,y}^V / (k \cdot T \cdot \Omega) \cdot \frac{\partial \mu}{\partial y} \end{cases} \quad (9)$$

177 where k is the Boltzmann's constant, T (K) is the absolute temperature, Ω (m³) is the
 178 atomic volume, μ (kJ·mol⁻¹) is the chemical potential, and $D_{eff,x}^V$ and $D_{eff,y}^V$ (m²/s) are the
 179 effective volume diffusion coefficients in the transverse and longitudinal directions,
 180 respectively. Hart [54] has shown that in presence of dislocation pipe diffusion
 181 mechanisms, the coefficient of bulk diffusion increases proportionally to the dislocation
 182 density. Due to the anisotropic plastic deformation of the particles, the value for pipe
 183 diffusivity is different in x and y:

184
$$\begin{cases} D_{eff,x}^V = D_V \left(1 + \pi \cdot r_p^2 \cdot d_{d,x} \cdot \frac{D_p}{D_V} \right) \\ D_{eff,y}^V = D_V \left(1 + \pi \cdot r_p^2 \cdot d_{d,y} \cdot \frac{D_p}{D_V} \right) \end{cases} \quad (10)$$

185 where D_V and D_p (m²/s) are the coefficient of volume diffusion and pipe diffusion in
 186 equilibrium conditions, respectively, r_p (μm) is the pipe radius, $d_{d,x}$ and $d_{d,y}$ (1/m²) are
 187 the dislocation densities along the two directions, x and y, respectively.

188 The relation between chemical potential and stresses is given by:

189

$$\begin{cases} \frac{\partial \mu}{\partial x} = -\Omega \cdot \frac{\partial \sigma_y}{\partial x} \\ \frac{\partial \mu}{\partial y} = -\Omega \cdot \frac{\partial \sigma_x}{\partial y} \end{cases} \quad (11)$$

190 Introducing Equations (10) and (11) into (9), the diffusion fluxes are given by:

191

$$\begin{cases} J_x^V = D_V \cdot \frac{\left(1 + \pi \cdot r_p^2 \cdot d_{d,x} \frac{D_p}{D_V}\right)}{(k \cdot T)} \cdot \frac{\partial \sigma_y}{\partial x} \\ J_y^V = D_V \cdot \frac{\left(1 + \pi \cdot r_p^2 \cdot d_{d,y} \frac{D_p}{D_V}\right)}{(k \cdot T)} \cdot \frac{\partial \sigma_x}{\partial y} \end{cases} \quad (12)$$

192 Substituting expressions (7) and (8) in (12) the diffusion fluxes can be rewritten as:

193

$$\begin{cases} J_x^V = 3 \cdot D_V \cdot \frac{\left(1 + \pi \cdot r_p^2 \cdot d_{d,x} \frac{D_p}{D_V}\right)}{(k \cdot T)} \cdot \gamma_{sv} \cdot \frac{1}{a} \cdot \left[\frac{1}{r_a} - \frac{1}{a} \sin\left(\frac{\phi}{2}\right) \right] \\ J_y^V = 3 \cdot D_V \cdot \frac{\left(1 + \pi \cdot r_p^2 \cdot d_{d,y} \frac{D_p}{D_V}\right)}{(k \cdot T)} \cdot \gamma_{sv} \cdot \frac{1}{c} \cdot \left[\frac{1}{r_c} - \frac{1}{c} \sin\left(\frac{\phi}{2}\right) \right] \end{cases} \quad (13)$$

194 On the other hand, the diffusional fluxes are proportional to the change in the contact
195 lengths between the powder particles, Δ_x and Δ_y as follows:

196

$$\begin{cases} J_x^V(a) = - \frac{d(\Delta_y)}{dt} \cdot \frac{a + a_p}{\Omega \cdot \frac{S_p}{2}} \cdot \delta \\ J_y^V(c) = - \frac{d(\Delta_x)}{dt} \cdot \frac{c + c_p}{\Omega \cdot \frac{S_p}{2}} \cdot \delta \end{cases} \quad (14)$$

197 where δ (nm) is the grain boundary thickness.

198 The strain rates along x and y can be written as:

199

$$\left\{ \begin{array}{l} \dot{\epsilon}_x = \frac{d(\Delta_x)}{dt} \cdot \frac{1}{(c+c_p)} \\ \dot{\epsilon}_y = \frac{d(\Delta_y)}{dt} \cdot \frac{1}{(a+a_p)} \end{array} \right. \quad (15)$$

200 Therefore, combining (14) and (15), a relationship between diffusion fluxes and shrinkage
 201 rates is obtained:

202

$$\left\{ \begin{array}{l} \dot{\epsilon}_x = -\frac{J_y^v(c)}{(a+a_p)} \cdot \frac{\left(\Omega \cdot \frac{S_p}{2}\right)}{\left[(c+c_p) \cdot \delta\right]} \\ \dot{\epsilon}_x = -\frac{J_x^v(a)}{(c+c_p)} \cdot \frac{\left(\Omega \cdot \frac{S_p}{2}\right)}{\left[(a+a_p) \cdot \delta\right]} \end{array} \right. \quad (16)$$

203 Let us consider the case of free pressure-less sintering. Plugging Eq.(13) into Eq.(16),
 204 the strain rates can be written as:

205

$$\left\{ \begin{array}{l} \dot{\epsilon}_x^{f.s} = -3 \frac{D_V \left(1 + \pi \cdot r_p^2 \cdot d_{d,y} \frac{D_p}{D_V}\right) \cdot \Omega}{k \cdot T \cdot \delta} \cdot \gamma_{sv} \cdot \frac{S_p/2}{c \cdot (a+a_p) \cdot (c+c_p)} \cdot \left[\frac{1}{r_c} - \frac{1}{c} \cdot \sin\left(\frac{\phi}{2}\right)\right] \\ \dot{\epsilon}_y^{f.s} = -3 \frac{D_V \left(1 + \pi \cdot r_p^2 \cdot d_{d,x} \frac{D_p}{D_V}\right) \cdot \Omega}{k \cdot T \cdot \delta} \cdot \gamma_{sv} \cdot \frac{S_p/2}{a \cdot (c+c_p) \cdot (a+a_p)} \cdot \left[\frac{1}{r_a} - \frac{1}{a} \cdot \sin\left(\frac{\phi}{2}\right)\right] \end{array} \right. \quad (17)$$

206 These strain rate equations can be used to obtain expressions of the shrinkage rates as
 207 functions of the geometric parameters of the porous material, diffusivities and deformation
 208 state.

209

210 3. Experimental procedure for model validation

211 In order to validate the proposed micromechanical model, a variety of experimental data
 212 was collected. The free-sintering strain rates were obtained from dilatometric tests, the

213 geometric features with image analysis of scanning electron microscopy images, and
214 detailed information on iron material properties were found in the literature. The
215 dislocation densities in the transverse and longitudinal directions are calculated based on
216 the work of Kuhn and Downey [15]. These dislocation density values become the model
217 validation parameters, comparing these calculated values with experimental values.
218 Dislocation densities can be experimentally derived with both nanoindentation and from
219 electron backscatter diffraction (EBSD) techniques. Nanoindentation allows the
220 estimation of the overall dislocation densities (statistically stored dislocations (SSDs) and
221 geometrically necessary dislocations (GNDs) with the only exception being those due to
222 the indentation process itself), but it is limited in accuracy when it comes to selecting the
223 most appropriate areas for the measurements. On the other hand, EBSD produces
224 detailed misorientation maps, from which dislocation density distributions can be derived,
225 but such values only include GNDs. Thus, in order to obtain accurate experimental data
226 for our model validation procedure, both nanoindentation and EBSD were performed. In
227 the results section (Section 4) a good correlation between modeling and experiments is
228 achieved, while in the following sub-sections the details of the various experimental
229 procedures are described.

230

231 **3.1 Dilatometric analysis**

232 A water atomized iron powder ($d_{25} < 45 \mu\text{m}$) was mixed with 0.6 wt% amide wax as
233 lubricant. Charpy bars [55x10x10 (mm)] with 6.9 g/cm^3 green density were produced by
234 uniaxial cold compaction (Höganäs AB, Höganäs, Sweden). After debinding at 500°C for
235 1h in an Ar atmosphere, parallelepiped-shaped samples [10x5x5 (mm)] were cut from the

236 Charpy bars along the compaction direction (y or longitudinal direction) and in the
237 compaction plane (x or transverse direction) as shown in Fig. 2.

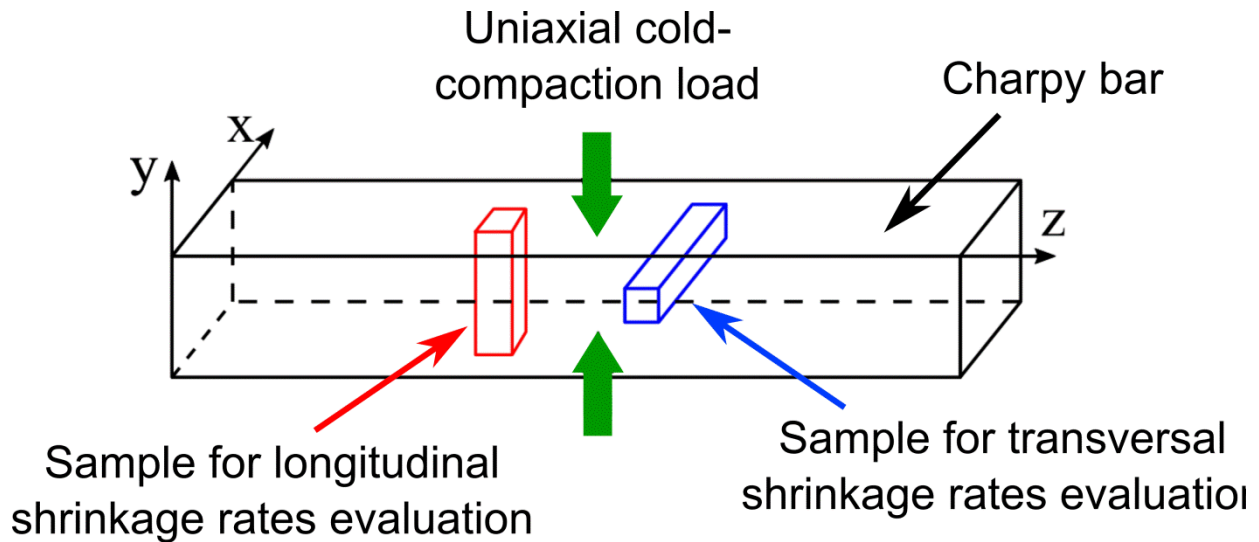


Fig. 2. Dilatometry samples for the longitudinal (y, in red) and transverse (x, in blue) shrinkage rates analysis, as derived from cold-pressed Charpy bars. The direction of uniaxial compaction is marked.

238 These samples were used in dilatometric experiments, in which the shrinkage kinetics
239 along the two directions could be measured. The specimens cut in such a way that the
240 long side corresponded to the y-axis in the Charpy bars (red in Fig. 2) provided data on
241 the longitudinal shrinkage rates ($\dot{\epsilon}_y^{f.s.}$), while the specimens with long sides aligned with
242 the x-axis of the Charpy bar (blue in Fig. 2) were used for the transverse shrinkage rates
243 ($\dot{\epsilon}_x^{f.s.}$).

244 The samples were isothermally sintered for 1 hour at different temperatures in the range
245 between 640°C and 1010°C, reached with a heating rate of 30°C/min. An example of
246 dilatometric curve is shown in Fig. 3, where the different shrinkages along the two
247 directions are presented and highlighted at the bottom.

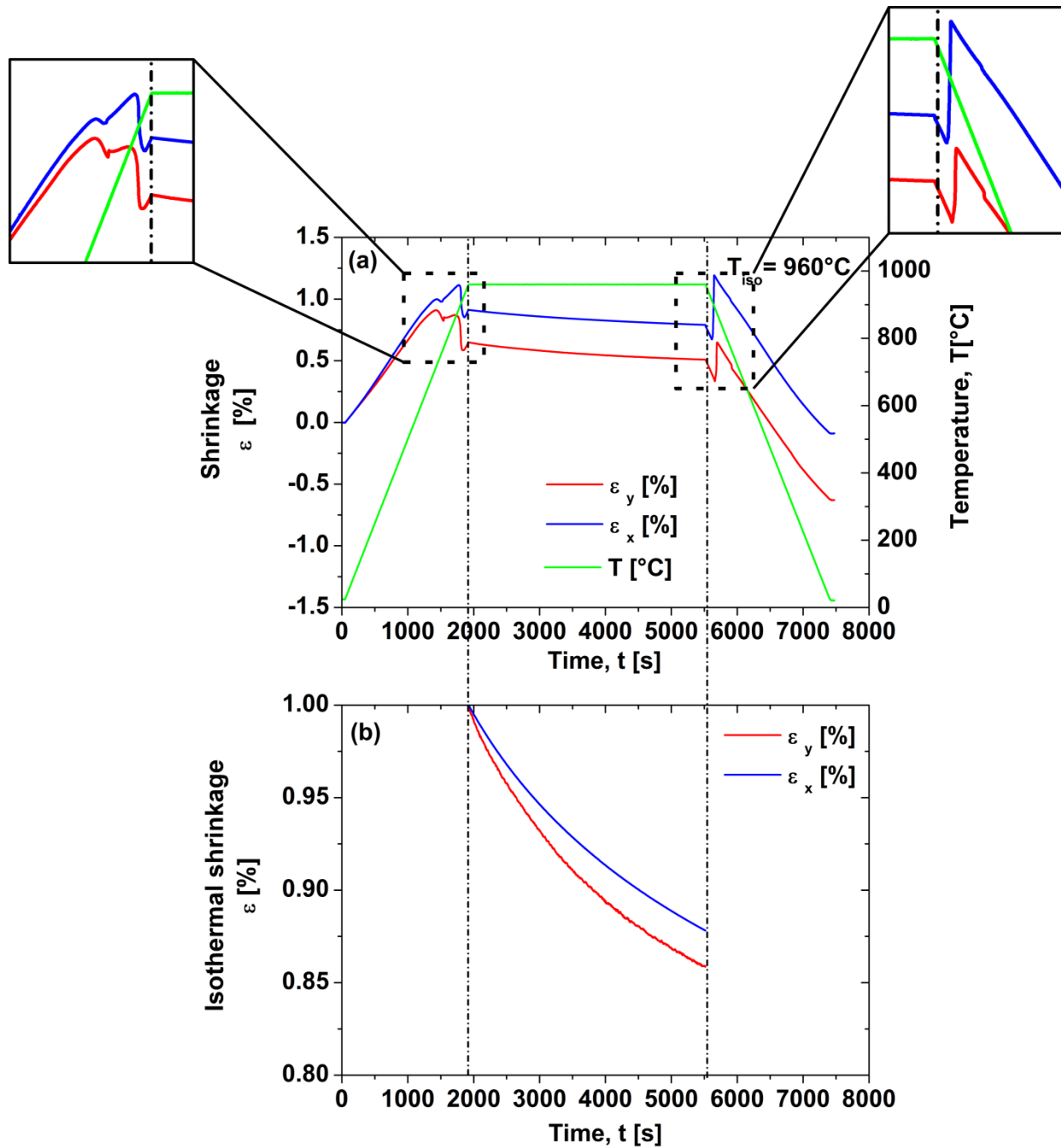


Fig. 3. Example of dilatometric curve for sintering with holding at 960°C: (a) temperature regime and shrinkages in the longitudinal (y) and transverse (x) direction for the entire processing route; (b) shrinkage curves during the isothermal holding time.

248 The additional step changes in shrinkage, both along x and y direction, marked in the
 249 top part of the same Fig. 3 before and after the isotherm segment, are related to well-
 250 known phase changes in iron. Specifically, at the Curie temperature ($T = 770^\circ\text{C}$) the

251 magnetic transformation leads to a steep increase of iron's self-diffusivity, and therefore
252 to a shrinkage enhancement (and correspondingly to a slight contraction during cooling)
253 [67-69]. At 910°C, on the other hand, the austenitic transformation also leads to a
254 shrinkage increase during heating and to a volume expansion upon cooling [52].

255

256 **3.2 Image analysis**

257 The surfaces of the sintered samples were prepared according to the standard
258 metallographic procedure and were observed in a scanning electron microscope (FEI
259 XL30 ESEM). The obtained micrographs were then processed with the image analysis
260 software ImageJ[®], in order to measure the various geometric characteristics of the
261 microstructure of the porous material, namely particle and pore semi-axes.

262 The method used to evaluate the extension of the particle semi-contacts a and c is
263 described in a previous work [49]. Fig. 4 shows an example of identification of the semi-
264 axis of a particle.

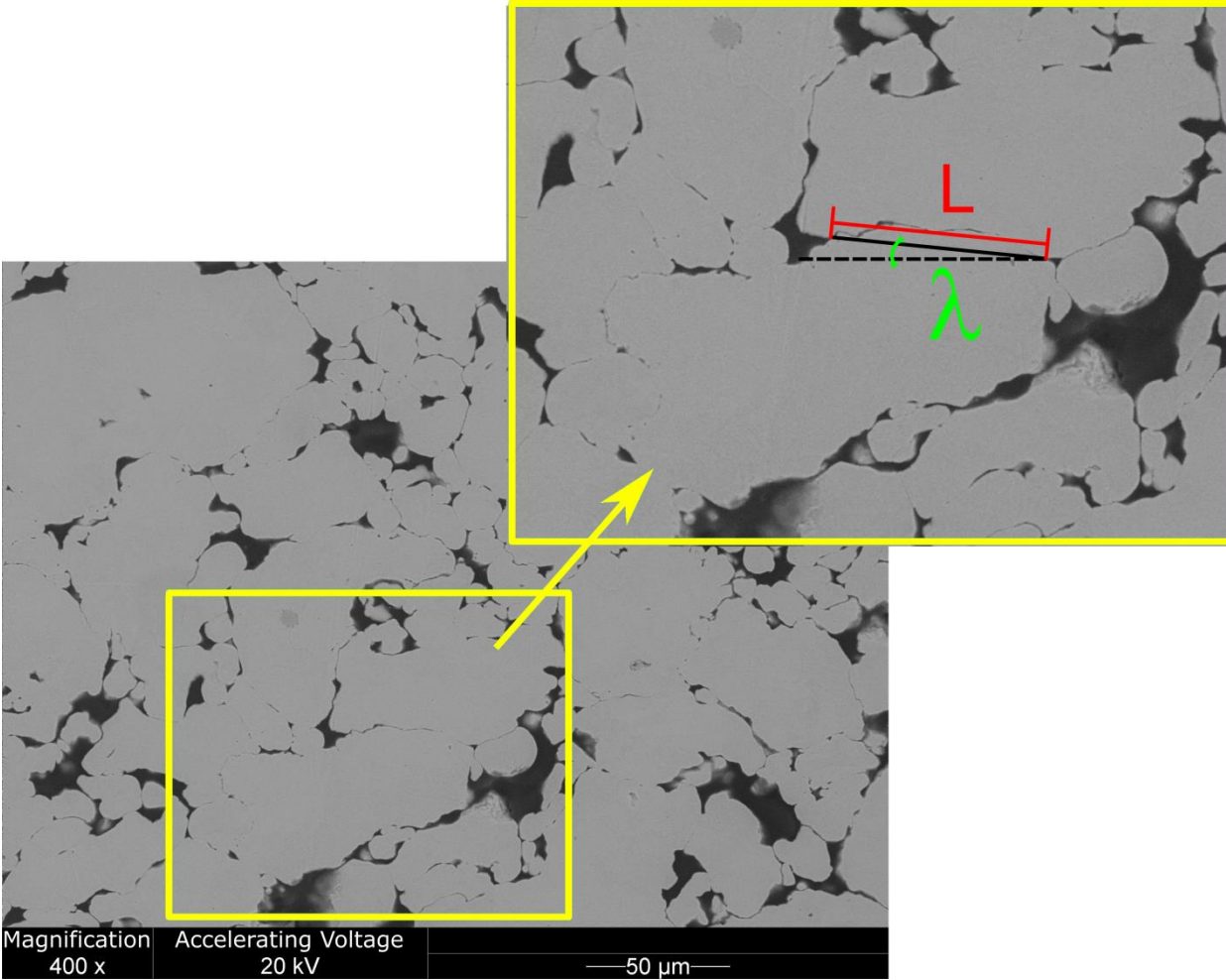


Fig. 4. Individuation of inter-particle contacts length (L) and inclination (λ) from image analysis of SEM micrographs.

265 The length L and the inclination λ with respect to the horizontal direction (lying in the
 266 compaction plane) of the inter-particle contact lines were measured, and the projections
 267 along directions x and y were calculated as:

268
$$\begin{cases} a = \frac{L}{2} \cos \lambda \\ c = \frac{L}{2} \sin \lambda \end{cases} \quad (18)$$

269 The pores semi-axes a_p and c_p were calculated based on the schematic presented in Fig.
 270 5.

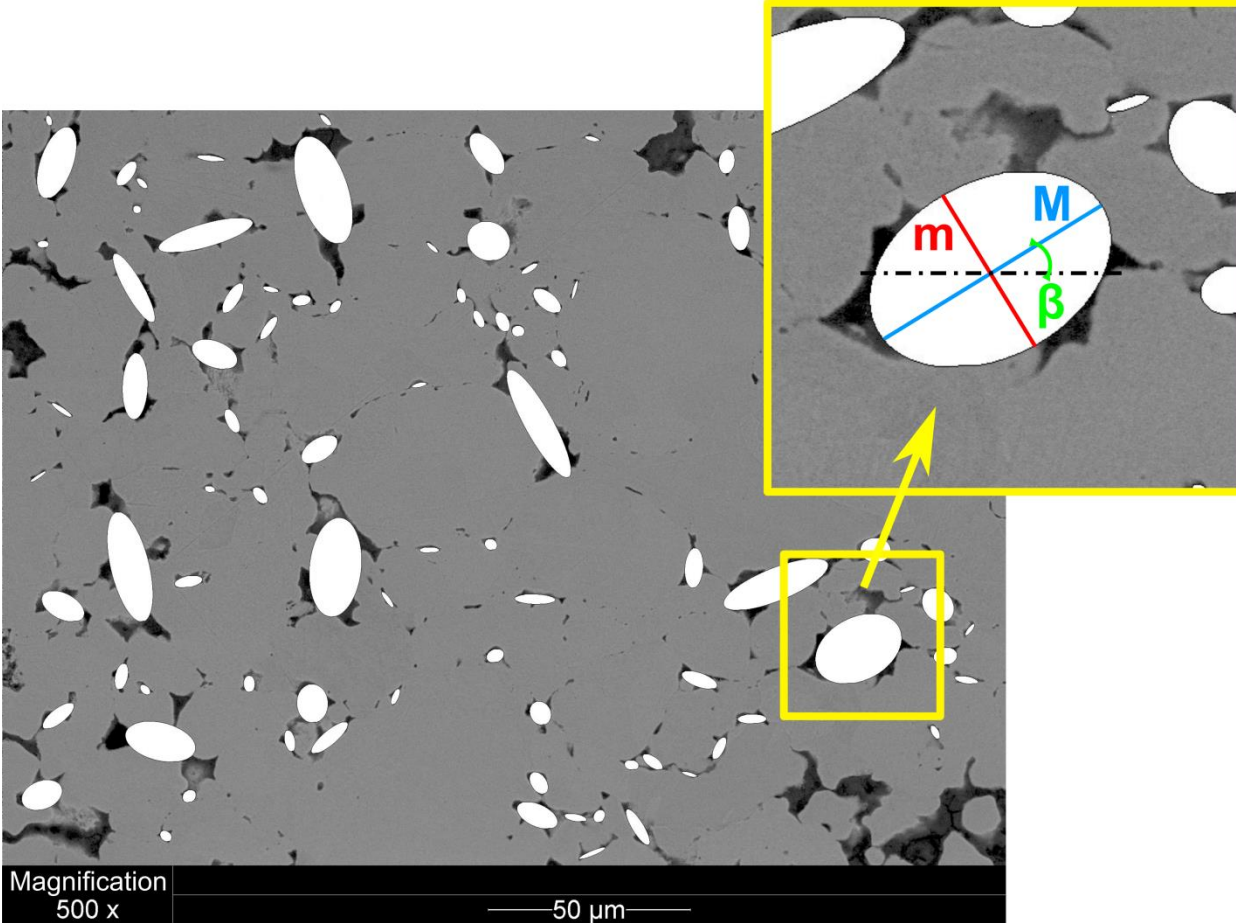


Fig. 5. Individuation of the pores' geometrical parameters from image analysis of SEM micrographs.

271 The shape of each pore is approximated as an ellipse with an area equivalent to its
 272 extension, according to the stereological approach. This allows obtaining reasonable
 273 mean values of the radii, which take into account both the small radii of pores at junctions
 274 with grain boundaries and the lower curvatures of larger voids. The average pore
 275 curvature values at grain boundary/pore junctions are related to the dihedral angle, which
 276 is generally well-known for a certain material system. Note, therefore, that even though
 277 the choice of the elliptical morphology is only an approximation, an appropriate value of
 278 the dihedral angle ($\phi = 157^\circ = 2.75 \text{ rad}$) has been taken into account in the model, as
 279 specified in Equation 5, and this leads to the results comparable with the experimental

280 values reported in literature [70]. The inclination of its major axis with respect to the
 281 horizontal direction of the image (β) provides the orientation of the pore. The pores that
 282 are not fully captured in the image are excluded from the analysis. The software returns
 283 the values of axes of the ellipses (M and m) and of the angle β . By using β to project the
 284 ellipses axes along longitudinal and transverse directions, the pores semi-axes a_p and c_p
 285 are calculated as:

$$286 \quad \begin{cases} 0 \leq \beta < 45^\circ : a_p = M \cdot \cos \beta; c_p = m \cdot \sin \beta \\ 45^\circ \leq \beta < 135^\circ : a_p = m \cdot |\cos \beta|; c_p = M \cdot \sin \beta \\ 135^\circ \leq \beta < 185^\circ : a_p = M \cdot |\cos \beta|; c_p = m \cdot \sin \beta \end{cases} \quad (19)$$

287

288 **3.3 Nanoindentation**

289 Hardness data from indentation tests can be used to estimate dislocation densities. In the
 290 present study, the choice of nanoindentation was imposed by the small dimensions of the
 291 iron powder particles, and the consequently restricted inter-particle contact areas, where
 292 the plastic deformation is assumed to be concentrated.

293 For nanoindentation analyses, the surface preparation is a critical step to get consistent
 294 experimental values. In order to obtain an optimal surface quality, the metallographic
 295 samples were polished using SiC papers with decreasing roughness, followed by
 296 polishing with 3- μm and 1- μm diamond paste, and finally with an OP-S suspension with
 297 0.04 μm diameter alumina particles. With this type of polishing procedure, it is possible to
 298 obtain results comparable to those typical of electrochemical polishing [71].

299 Nanoindentation was performed on samples pressureless sintered at 640°C, 730°C,
 300 860°C, and 960°C. Three different indentation forces (55 mN, 75 mN and 95 mN) were
 301 employed, with a 20-s hold before unloading. The measurements were carried out in the

302 contact areas aligned along the x and y directions, and not in ambiguously oriented ones,
303 in order to observe the state of deformation in these two distinct regions of the porous
304 material. Fig. 6 shows an example of micrographs of nanoindentation for each direction.

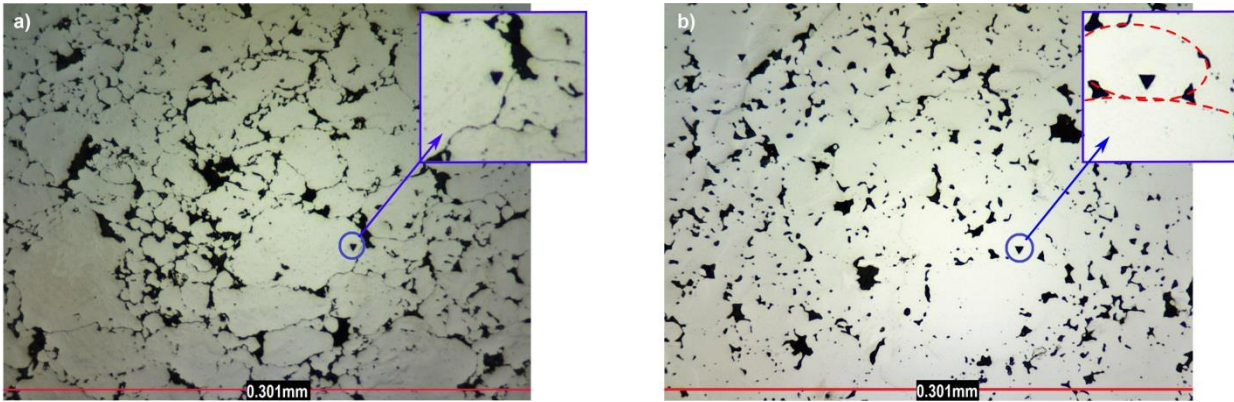


Fig. 6. Examples of micrographs of nanoindentation tests: (a) with 55 mN load on a sample sintered at 640°C (for a longitudinal contact); (b) with a 95 mN load on a sample sintered at 960°C (for a transverse contact). In the latter case the two involved powder particles have been highlighted.

305

306 **3.4 Electron Backscatter Diffraction (EBSD)**

307 EBSD is a technique performed in the SEM that allows direct measurement of the lattice
308 orientation in crystalline materials. Lattice orientation can, in turn, be related to dislocation
309 density. Here the experimental procedure is described, and in Section 4.4 the dislocation
310 densities calculation is presented.

311 The iron samples sintered at 640°C, 730°C, 860°C and 1010°C were mounted in hot
312 resin. Grinding was performed at 300-rpm under a force of 20N for 5 minutes through
313 220, 600 and 1200 grit. Polishing was performed at 150-rpm under a force of 15N for 5
314 min using 3- μ m diamond suspension, 10 min using 1- μ m diamond suspension, and 10N
315 force for 20 min using 0.04- μ m colloidal silica solution. A finishing polish step was then
316 applied for 60 min using the colloidal silica activated disk and deionized water under a
317 force of 5N.

318 Prior to EBSD imaging in the SEM, we carried out a step size analysis and determined
 319 an appropriate step size to be ~200nm for the EBSD scans reported herein. Furthermore,
 320 in order to present valid GND results, the lower bound of log₁₀ GND density is estimated,
 321 *i.e.* noise floor at a step size of 200nm, to be 9.93×10^{13} per m², and this value is used as
 322 a lower bound filter for GND post-processing. A misorientation threshold is set to 2° to
 323 filter out GND calculated from minimum misorientation of non-indexed points or
 324 neighboring grains. The misorientation mask also produced clear-cut grain boundaries
 325 and an average disorientation (*i.e.* minimum misorientation) angle map that can be readily
 326 visualized, as shown in Fig. 7.

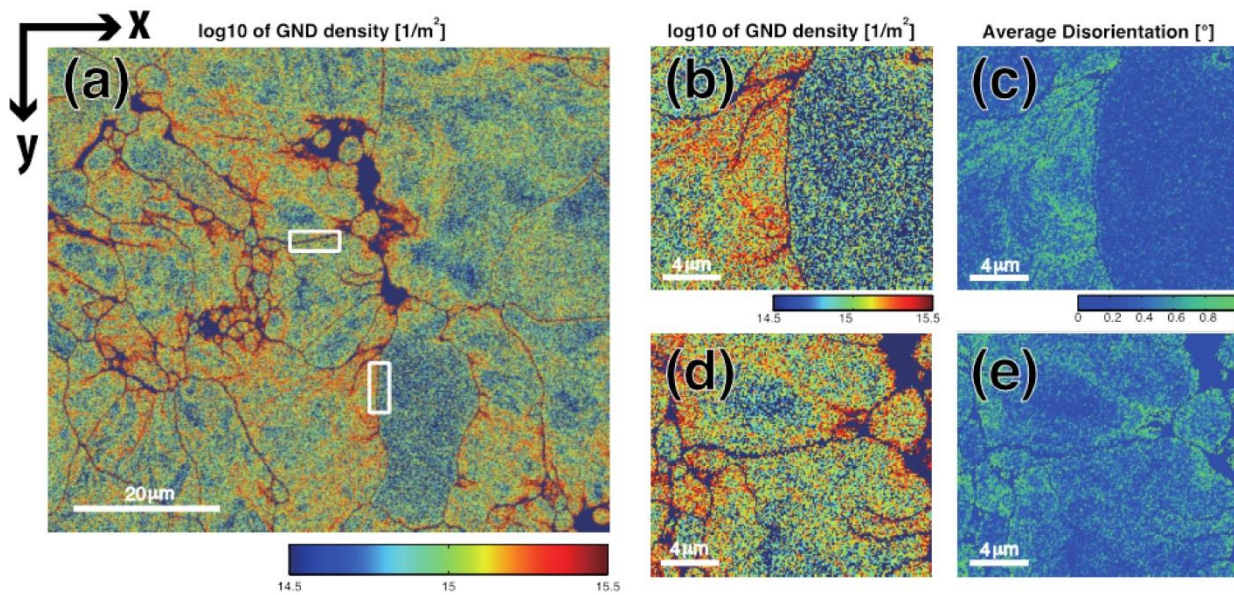


Fig. 7. Example of EBSD results for GND density distribution (measured as log₁₀ of GNDs per m²) and average disorientation angle distribution: (a) GND density distribution for a sample sintered at 1010°C, acquired at 2000X and with 200 nm step size, with selection of boxes around representative x and y inter-particle contacts; (b) GND density along y and (d) along x; (c) average disorientation angle distribution around an inter-particle boundary along y and (e) along x.

327 The GND analysis of inter-particle boundaries can be summarized to be a four-step
 328 procedure, presented schematically in Fig. 8.

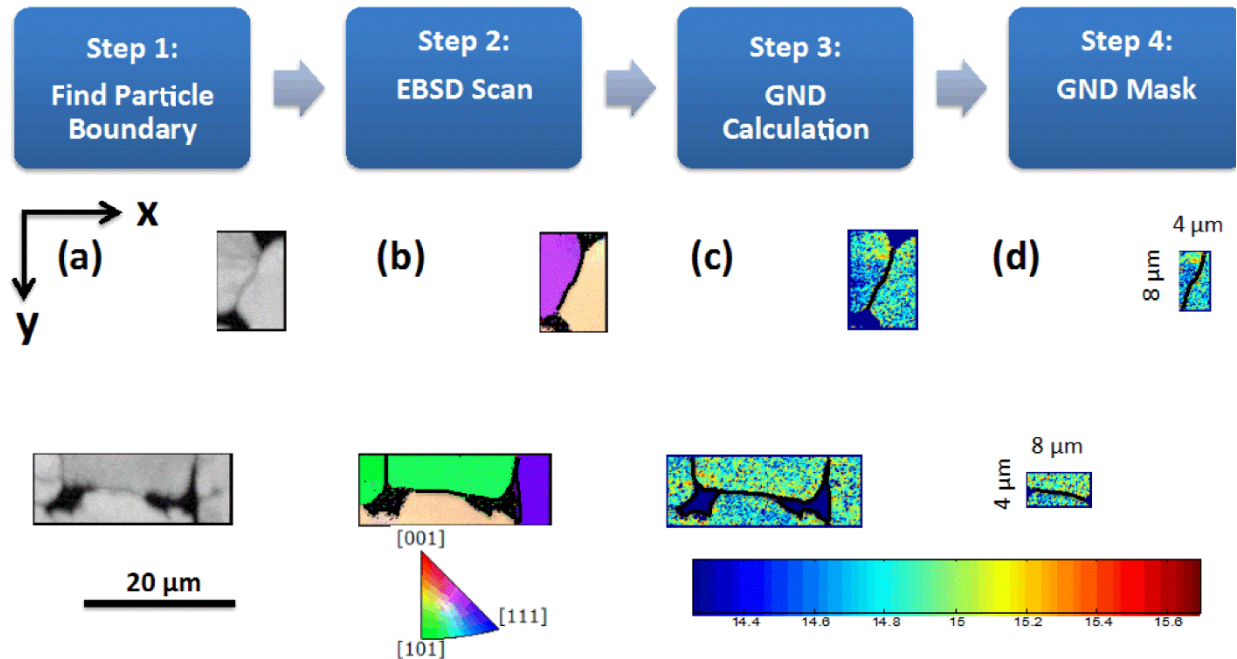


Fig. 8. Steps followed for the EBSD analysis of a sample sintered at 1010°C: (a) pattern quality image showing the individuation of longitudinal and transverse particle boundaries based on pores at triple junctions; (b) EBSD scan of the pre-selected regions; (c) GND density map around the particle boundaries; (d) particle boundary selection refinement with an 8x4 μm box.

329 The EBSD imaging was conducted on a FEI Quanta 600 SEM, equipped with a Bruker
 330 e-Flash EBSD system, operated at 20kV, with a 1x1 binning size and working distance
 331 of ~15 mm. The inter-particle boundaries were pre-selected on the forward-scattered
 332 electron image collected by a detector roughly 25mm from the sample surface. Typically,
 333 as demonstrated in Fig. 8, particle contacts could be readily identified near two pointed-
 334 pores (namely particle boundary triple-points). Then, the detector distance was reduced
 335 to ~15mm and masked areas were placed on the selected particle boundaries for EBSD
 336 scans. Three scans per sample were taken at a step size of 200nm at different locations
 337 in the proximities of the center of the sample. Approximately 15 horizontal and 15 vertical
 338 particles contacts were considered for every sample (30 for every sample, 120 in total).
 339 To minimize the EBSD scan time, instead of analyzing the entire sample, EBSD scans

340 were performed only on selected area in the masked zones over the contact boundaries.
341 In each case of particle boundaries selection, the masking boxes were set to have the
342 short side (across the particle contact) equal to $4\mu\text{m}$, and the long side (along the contact)
343 equal to $8\mu\text{m}$, as shown in Fig. 8. The selection of the short side size was the most critical,
344 because it implied an assumption on the extent of the plastically deformed zone.
345 Qualitative considerations based on the previously conducted nanoindentation analyses
346 were combined to the image analyses results, until $2c_p$ ($\approx 4\mu\text{m}$), with c_p being the smallest
347 geometric parameter involved in this study. Centering of the boxes on the particle
348 boundaries was performed manually from the EBSD images to accurately locate the
349 particle boundary in the EBSD scan.

350

351 **4. Results and discussion**

352 **4.1 Dilatometric analysis**

353 From the dilatometric curves the shrinkage rates in the transverse and longitudinal
354 directions, $\dot{\epsilon}_x^{f.s.}$ and $\dot{\epsilon}_y^{f.s.}$, could be calculated. Fig. 9 shows that the absolute values of
355 shrinkage rates progressively decrease during the isothermal holding time-step.

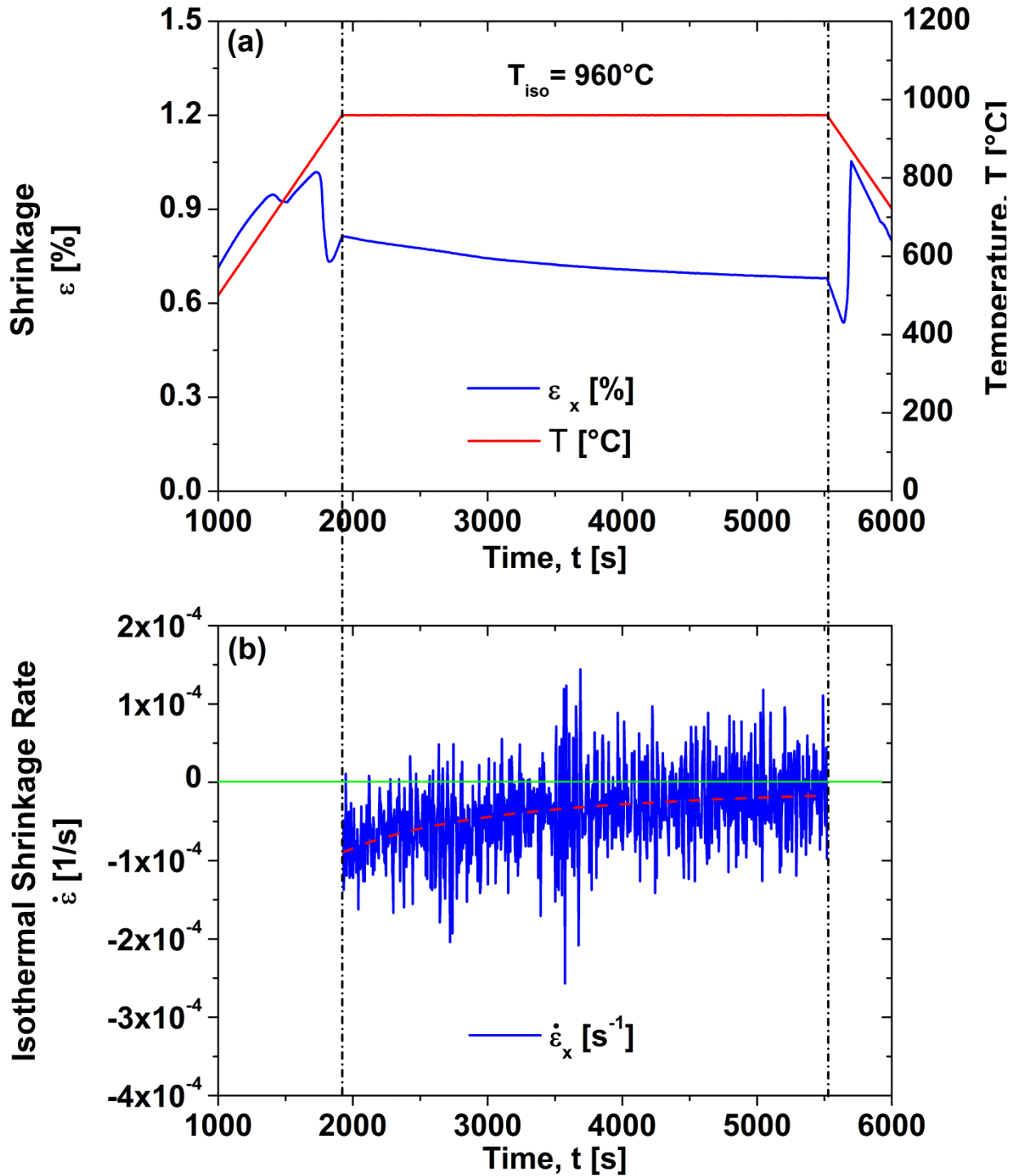


Fig. 9. Example of derivation of isothermal shrinkage rate in the transverse direction, $\dot{\varepsilon}_x(t)$, for a sample sintered at 960°C. (a) Dilatometric curve with isothermal part highlighted between dashed lines; (b) corresponding isothermal shrinkage rate.

356 An integral average was therefore calculated, as:

357

$$\left\{ \begin{array}{l} \bar{\dot{\epsilon}}_x^{f.s} = \int_0^t \dot{\epsilon}_x^{f.s}(t) \cdot dt / t^* \\ \bar{\dot{\epsilon}}_y^{f.s} = \int_0^t \dot{\epsilon}_y^{f.s}(t) \cdot dt / t^* \end{array} \right. \quad (20)$$

358

where t^* (s) is the time at which $\dot{\epsilon}_x^{f.s}(t)$ and $\dot{\epsilon}_y^{f.s}(t)$ approach zero.

359

The obtained values for the various sintering temperatures are given in Table 1.

360

As expected, the shrinkage rates are higher along the compaction direction (in absolute

361

value) than along the transverse one. Below the Curie point ($T = 770^\circ\text{C}$), the difference

362

between the two directions is most noticeable and shows a significant increase with

363

increasing temperatures. Such a difference is still evident between the Curie point and

364

the temperature of the austenitic transformation ($T = 910^\circ\text{C}$), while it becomes almost

365

negligible in the austenitic field, probably due to recrystallization and recovery

366

phenomena. Increasing sintering temperatures also lead to noticeable changes in the

367

value of the average shrinkage rates. Between 640°C and 860°C , the expected increase

368

in absolute densification rate is observed when the isothermal temperature increases.

369

The increase is particularly sharp between 640°C and 730°C , due to the magnetic

370

transformation, which greatly increases the self-diffusivity of iron starting around 680°C

371

[67]. The shrinkage rates subsequently drop when 960°C is reached, due to the austenitic

372

transformation. Switching from a BCC to an FCC phase acts as an annihilation of plastic

373

deformation, and thus the pipe-diffusion effect is reduced. Raising the temperature to

374

1010°C then provides additional energy to the process, and therefore enhances

375

densification again. Since in Table 1 only the densification rate during isothermal hold is

376

considered, another reason for the observed changes in the absolute densification rate

377

is that the starting density at the onset of isothermal sintering is different in all these

378 samples (increasing as the temperature increases). The focus on the isothermal segment
379 allowed the exclusion of thermal expansion effects from the present study. Nevertheless,
380 the partial shrinkage occurring during the heating ramp led to the varying densities at the
381 onset of the isothermal hold, depending on the selected processing temperatures. The
382 concurrent effects of shrinkage and thermal expansion upon heating is the object of an
383 extension of the present study. The cooling stage was also analyzed, and it was assessed
384 that only the expected thermal contraction occurred, with no traces of additional shrinkage
385 and anisotropic behavior in the samples.

386

387 **4.2 Image analysis**

388 Figures 10 and 11 present the estimations of inter-particle contacts and pores semi-axes
389 lengths, respectively.

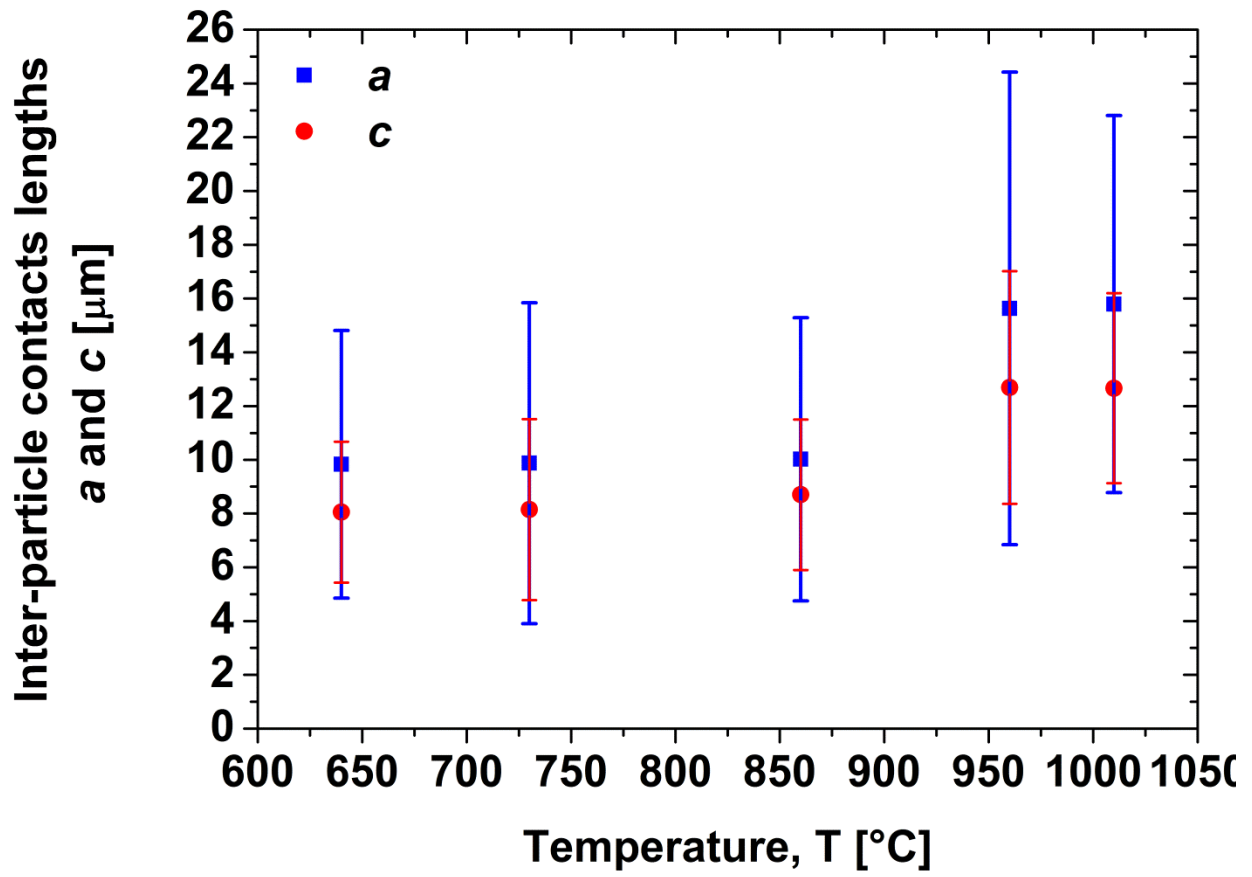


Fig. 10. Inter-particle contact lengths a and c at the various sintering temperatures.

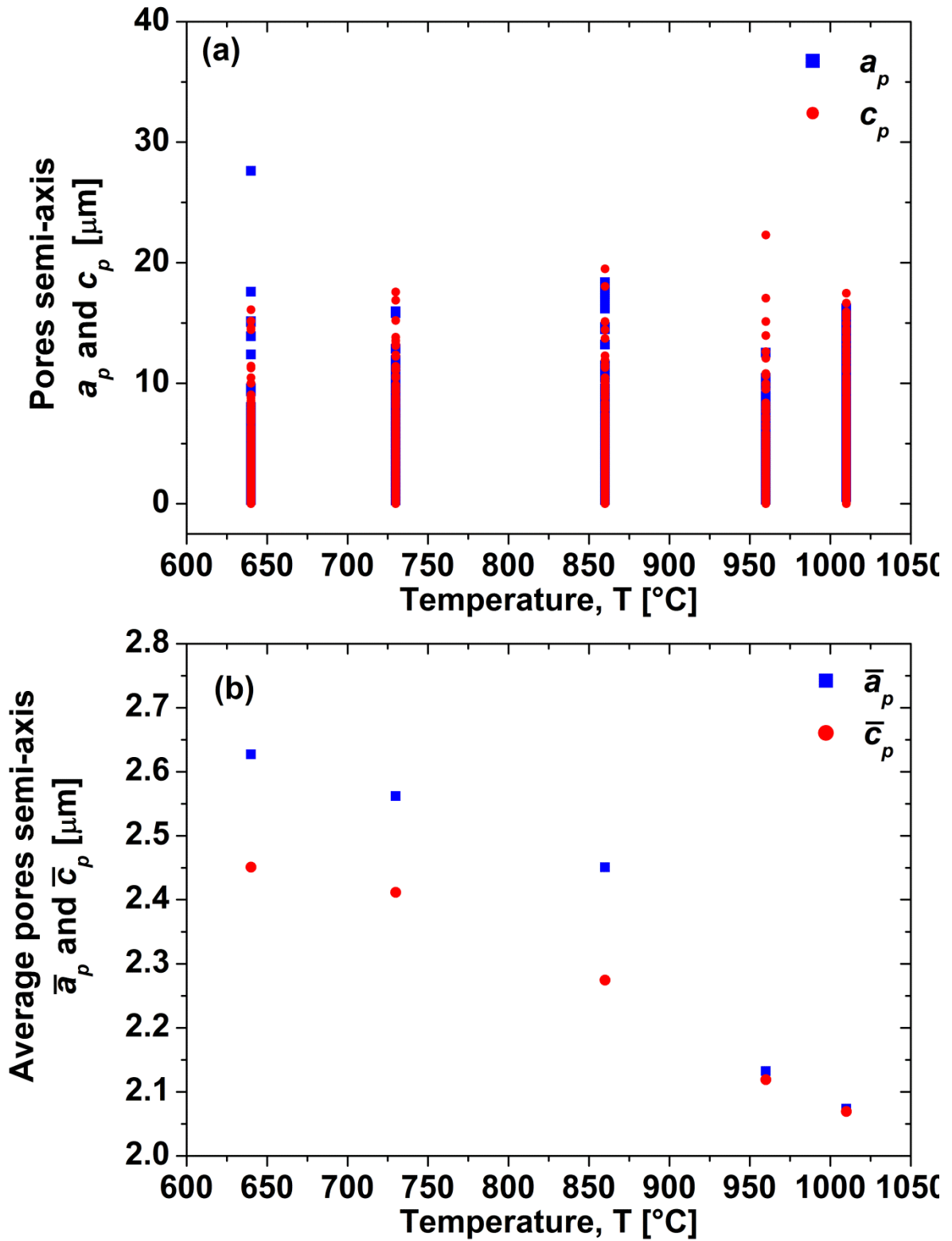


Fig. 11. Pores semi-axes lengths, a_p and c_p , at the different temperatures (a) values obtained from image analyses; (b) average values \bar{a}_p and \bar{c}_p .

391 In all the considered cases, the semi-axes perpendicular to the compaction direction are
392 greater than those parallel to it, confirming the anisotropy of the porous material due to
393 the pre-sintering cold pressing. This is more evident for the inter-particle contacts than in
394 the pores semi-axes case. For clarity, Fig. 11 also shows the average of the measured
395 values, \bar{a}_p and \bar{c}_p . It can be seen that the extension of the pores in the compaction
396 direction is lower than in the transverse plane at every sintering temperature, but the
397 distinction is less prominent at higher sintering temperatures, in accordance with
398 dilatometry results. The pore semi-axes data has been used to calculate the curvature of
399 the pores through Equation (1), leading to values in the range of 2.1-2.8 μm , depending
400 on the direction and temperature.

401

402 **4.3 Nanoindentation**

403 The first set of dislocation density data needed to verify the reliability of our model was
404 derived from the nanoindentation results, through the indentation size effect (ISE) model
405 developed by Nix and Gao [60–62]. This method uses Taylor’s nonlocal theory of
406 plasticity [75], according to which, for indentation tests at the micro and nano-scales, the
407 depth of the indent and the measured hardness values show a strong correlation for
408 depths less than 1- μm . In crystalline materials, this correlation is influenced by a
409 characteristic material parameter, called material length scale, which depends on the
410 deformation state of the sample under examination [73,74].

411 The nanoindentation hardness values and the corresponding indentation depths,
412 reported in Table 2, served as input for the main ISE equation, namely:

413
$$\frac{H}{H_0} = \sqrt{1 + h^*/h} \quad (21)$$

414 where H (GPa) is the experimental value of the hardness, H_0 (GPa) is the hardness due
415 to pre-existing dislocations, namely not due to the indentation process itself, h (μm) is the
416 depth of the indentation, and h^* (μm) is the characteristic depth of the material above
417 which we do not have any correlation between indentation depth and nanoindentation
418 hardness values. The highest and lowest measured H values are discarded, in order to
419 utilize more reliable experimental data.

420 Equation (21) can be rearranged as:

$$421 \quad H^2 = H_0^2 \cdot \left(1 + \frac{h^*}{h}\right) \quad (22)$$

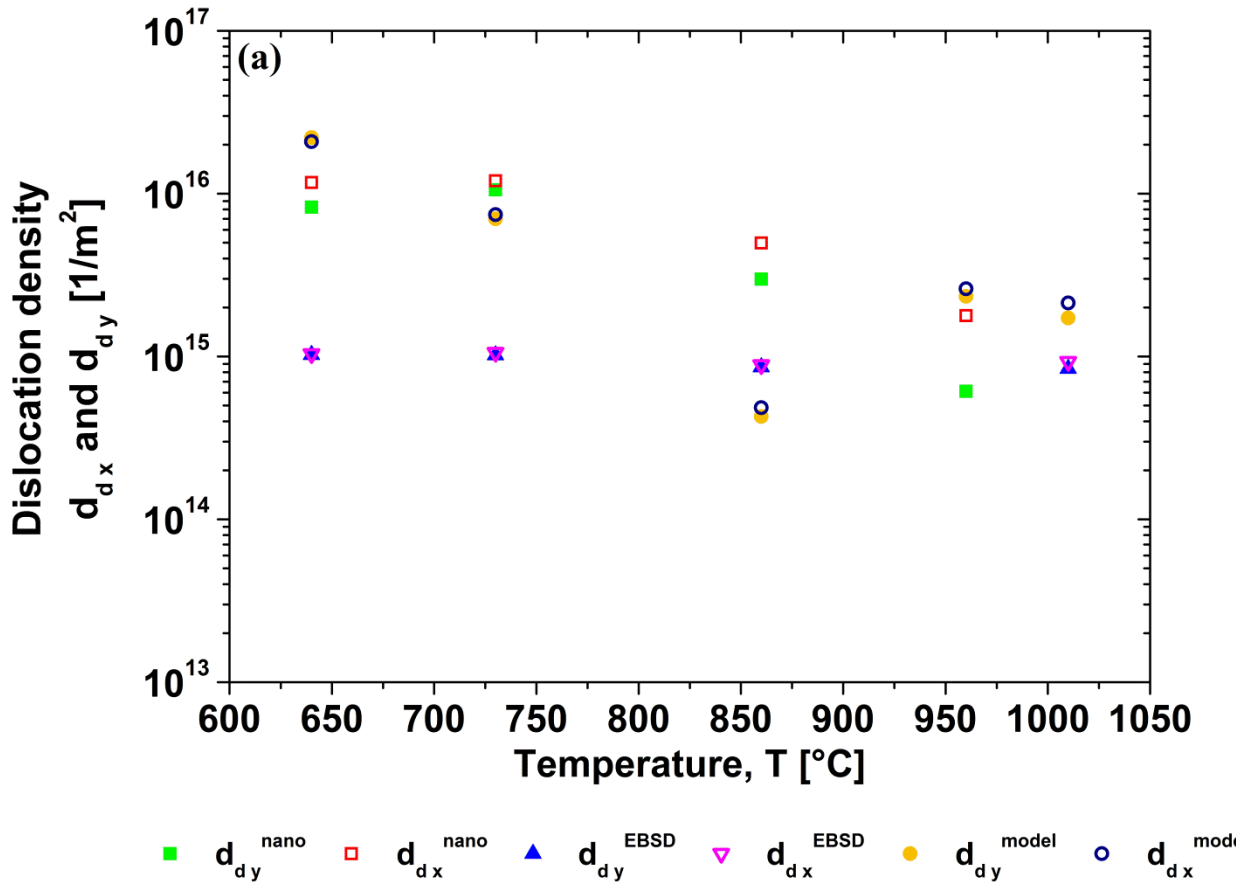
422 such that the plot of H^2 versus $1/h$ will consist of a straight line with slope proportional to
423 h^* and intercept corresponding to H_0^2 .

424 The dislocation density can subsequently be estimated with the following relation [73,74]:

$$425 \quad d_d = \frac{3 \cdot \bar{r} \cdot \tan^2 \theta}{2 \cdot b \cdot h^*} \quad (23)$$

426 where \bar{r} is the Nye factor (set as 1 due to negligible macroscopic plastic strain gradient
427 produced during cold compaction of powder), θ is the angle of contact between the
428 indenter tip and the sample surface (24.73° for Berkovich tips, utilized in the present case)
429 and b is the Burger's vector modulus (2.49\AA).

430 The results obtained for the different temperatures and directions are presented in Tab.
431 4 and Fig. 12.



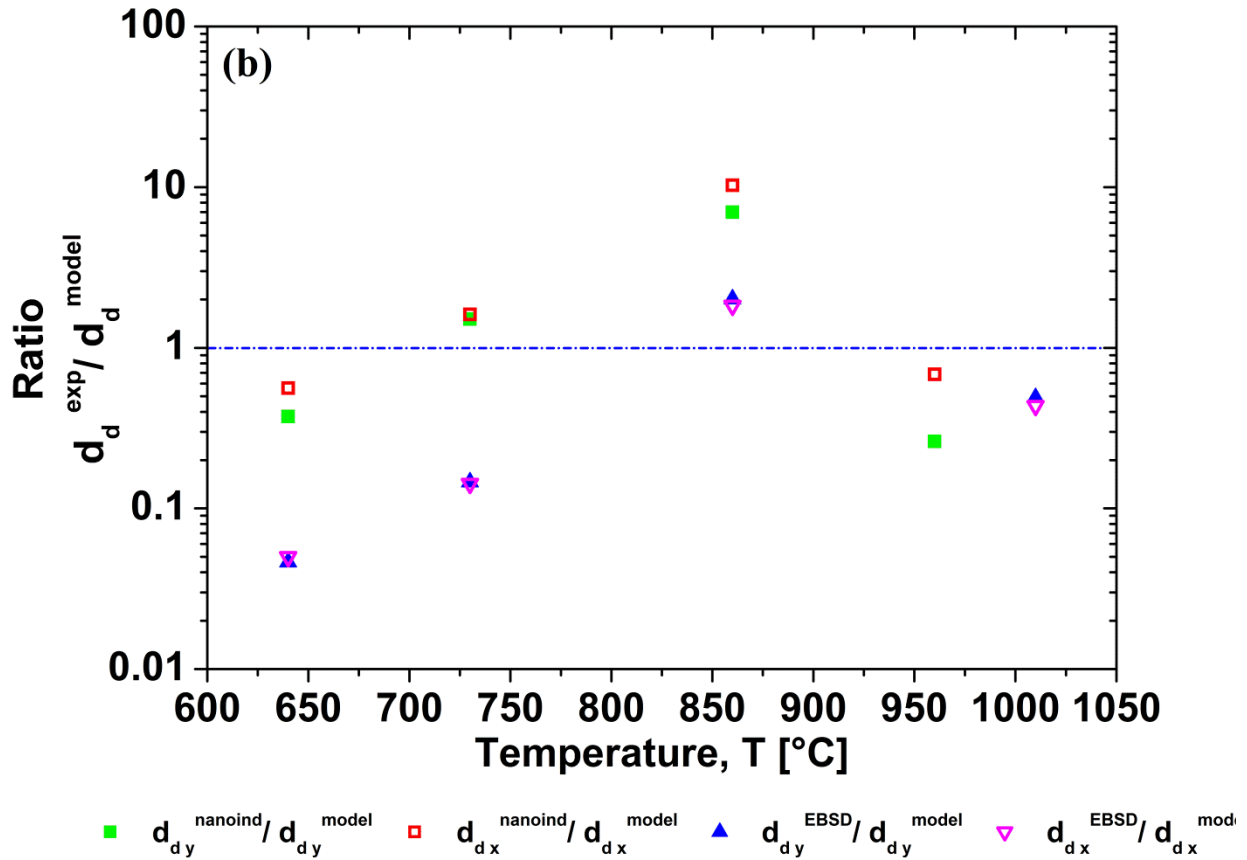


Fig. 12. Dislocation density values: (a) comparison between experimental and modeling results; (b) ratio between experimental and modeling results.

432 The expected higher amount of plastic deformation in the plane perpendicular to the cold
 433 compaction direction is confirmed: the dislocation densities are higher in the transverse
 434 contacts (d_{dx} , responsible for the shrinkage along the y direction) than in the longitudinal
 435 ones (d_{dy} , responsible for the shrinkage along x). With increasing sintering temperatures,
 436 the dislocation densities tend to increase until the Curie point is reached, because of the
 437 local deformations induced by the rising sintering stresses at the necks between the
 438 ductile iron powder particles, as reported also by Schatt and Friedrich [14]. After the Curie
 439 point, dislocation densities steadily decrease, likely because of the annealing and
 440 consequent recrystallization and recovery of the deformed material, leading to a less

441 marked anisotropy. These observations further confirmed the dilatometry and image
442 analysis observations.

443

444 **4.4 EBSD**

445 The second set of dislocation density data was obtained from the EBSD analysis [65].
446 With this technique only geometrically necessary dislocations (GNDs) are detected, and
447 not statistically stored dislocations (SSDs). Nevertheless, it is expected valuable
448 information can be obtained, since the high ductility of iron and the elevated load applied
449 during cold compaction generally lead to the generation of significant amounts of GNDs,
450 compared to the pre-existing SSDs.

451 The theory for the determination of GND density from EBSD data was adopted from the
452 work of Nye, relating lattice curvature to the dislocation density tensor, often itself denoted
453 as the Nye tensor [78]. Taking into account the elastic strain (ϵ_{ij}^{el}), according to Kröner,
454 the Nye/Kröner relation can be written as [76]:

$$455 \quad \alpha_{ik} = k_{ki} - \delta_{ki} k_{mm} - \partial_{klj} \frac{\partial \epsilon_{ij}^{el}}{\partial x_l} \quad (24)$$

456 where k_{ij} is the lattice curvature tensor and α_{ij} is the Nye tensor. In cases where the
457 plastic distortion of the lattice is assumed to be fully accommodated by lattice rotation,
458 *i.e.* negligible elastic strain, the dislocation density tensor can be approximated as the curl
459 of the lattice misorientation matrix) ($\Delta\phi = g_B g_A^{-1}$) in the following way [77]:

$$460 \quad \alpha_{ik} \approx -\partial_{kli} \Delta\phi_{ij,l} \quad (25)$$

461 The lattice orientation tensor (g) is directly measurable by the electron backscatter
462 diffraction (EBSD) technique in the SEM. For 2-D EBSD analysis, the orientation gradient

463 in the out of plane direction is assumed to be zero, such that the GND density calculated
 464 here is a lower bound solution of the actual GND density. Techniques such as serial-
 465 sectioning [78] and X-ray microbeams [79] have been developed to extract lattice
 466 orientation in the out of plane direction, but these techniques are usually complex and
 467 time-consuming.

468 On the other hand, the total GND density tensor can also be represented as the sum of
 469 individual dislocations, where each type of dislocation is geometrically characterized by
 470 a combination of the unit line vector \hat{l} and its Burger's vector b :

$$471 \quad \alpha_{ij} = \sum_{n=1}^{N=16} \rho_{GND}^n \cdot b_i^n \hat{l}_j^n \quad (26)$$

472 The dislocation configurations available in a bcc crystal are 4 screw $\langle 111 \rangle$ dislocations
 473 and 12 edge $\langle 111 \rangle \{110\}$ dislocations. This allows the number of dislocations present in
 474 the lattice to accommodate the measured lattice curvature to be calculated. The solution
 475 to this underdetermined system of equations, with 16 unknowns and 9 equations, is
 476 obtained through a so called 'interior-point' method based on an L^1 dislocation energy
 477 minimization scheme [80]. In practice, the 32 unknowns of dislocations densities (both
 478 positive and negative dislocations) are calculated, and the solution folded back to give
 479 the 16-component dislocation density vector.

480 Lattice misorientation data were obtained in images of the type presented in Fig. 8. Image
 481 post-processing, as well as GND calculations, were then conducted with the Optimization
 482 Toolbox of the MathWorks™ Matlab Program. The mean value of the GND density at the
 483 particle boundaries was obtained by dividing the sum of the total GND density for all data
 484 points near the particle boundary by number of data points with non-zero GND density.
 485 This approach allows the dislocation gradient from the particle interior to the boundary to

486 be calculated. To rule out large statistical variations, we have ignored the maximum and
487 minimum obtained values of mean GND density. Average dislocation density values in
488 the x and y directions and for each sintering temperature were then computed. The
489 obtained results are displayed in Fig. 12. A good correlation with the dislocation density
490 from the nanoindentation hardness data is observed, with EBSD-estimated dislocation
491 density values just below the nanoindentation hardness values. This is in accordance with
492 the fact that EBSD does not detect statistically stored dislocations. In addition, pipe
493 diffusion is mainly through SSDs at low sintering temperatures and through GNDs at high
494 sintering temperatures. This is due to the higher mobility of SSDs (which create a less
495 severe atomic lattice distortion with respect to GNDs), while diffusion through GNDs
496 requires more elevated temperatures in order to have a significant impact on
497 densification. The total dislocation density approached the GND's density at increasing
498 temperatures, which implies thermal annihilation of SSDs. At such temperatures, the
499 mobility of GND's is also high enough for them to contribute to the material's sintering,
500 while the SSD's role becomes decreasingly important. It is interesting to point out that,
501 different from nanoindentation results, all EBSD-derived dislocation density values are
502 close to the 10^{15} value, because GNDs are less sensitive to changes in sintering
503 temperature. This appears to be a maximum for most EBSD analyses, and is in
504 reasonable agreement with the fact that inter-particle boundaries can only allow a limited
505 amount of local lattice misorientation.

506

507 **4.5 Model validation**

508 The micromechanical model can now be validated by comparing the experimentally
509 obtained dislocation density data with those calculated from the model using equations
510 (17). Experimental data on shrinkage rates (section 4.1) and geometric parameters
511 (section 4.2) along x and y were obtained previously. The other input data needed are
512 iron material properties taken from the literature. Specifically, the inputs are:

- 513 - γ_{sv} , surface tension: 2.525 N/m [81,82];
- 514 - γ_{ss} , grain boundary energy: 0.985 N/m [83];
- 515 - δ , inter-particle boundary thickness, estimated as grain boundary thickness: 0.5
516 nm [84];
- 517 - r_p , pipe radius: 0.5 nm [67];
- 518 - Ω , atomic volume: $8.38 \cdot 10^{-30} \text{ m}^3$ [85].

519 Additionally, the values of the volume diffusion coefficient D_v as a function of the sintering
520 temperature were taken from [86] and are given in Table 3. In Table 3, the dislocation
521 pipe diffusion coefficient D_p values, obtained from Stechauner and Kozeschnik [87],
522 based on an Arrhenius-type relation, $D_p = D_0 \exp(-Q/RT)$, with activation energy Q
523 (kJ/mol) and pre-exponential factor D_0 (m^2/s) changing for the different iron phases, are
524 reported. The calculated pipe diffusivity values are comparable with the experimental
525 results measured by Shima *et al.* [67] at all temperatures, with the only exception of the
526 austenitic field, for which, to the best of our knowledge, data is not available in the
527 literature.

528 Note that, even though the model here is assessed with data on the free pressureless
529 sintering of pure iron, its applicability can be extended to a variety of material systems,
530 provided the data listed above. The utilization of the continuum theory of sintering also

531 allows for the possibility of including the role of externally applied pressures, by adding
532 the opportune term to the equations set. Thanks to its structure, it is also possible to
533 compare or connect with other sintering models present in literature, for instance, with the
534 meso-scale discrete elements-based simulations [88].

535 Substituting all the data listed above in equations (17), we could calculate estimations of
536 dislocation densities in the transverse (x) and longitudinal (y) directions for the various
537 sintering temperatures. Fig. 12 shows the comparison between the calculated and
538 experimentally obtained dislocation densities at different temperatures. A good
539 agreement is observed, with the only exception of $T = 860^{\circ}\text{C}$, at which nanoindentation
540 and EBSD results are fairly close to each other, while the model seems to underestimate
541 the amount of plastic deformation. This particular temperature, however, belongs to a
542 range between Curie and austenitic point in which the literature data for dislocation pipe
543 diffusivity are widely scattered and most likely often overestimated. Such uncertainty
544 might be responsible for the mismatch between modeling and experimental framework at
545 this particular temperature.

546 In order to verify this hypothesis, a parametric study was performed, by assessing the
547 effect of a change in the different variables involved in equations (17) on the calculated
548 dislocation density values. This analysis allows analyzing the sensitivity of the model to
549 the various parameters involved, by observing the changes in its response when the
550 parameters are altered within a reasonable range. The parameters taken into
551 consideration for this part of the study were pipe diffusivity, bulk diffusivity, strain rates,
552 particle semi-contact lengths and pore semi-axes. They were all changed within a certain
553 range, selected as follows. For the parameters that had been measured experimentally

554 (shrinkage rates, particle semi-contact lengths and pore semi-axes), the standard
 555 deviation was taken as a reference for the variation of each parameter. Specifically, the
 556 value of each parameter was altered by adding or subtracting 50% and 100% of their
 557 standard deviation value. For the parameters that had been taken from the literature (pipe
 558 and bulk diffusivities), the data were changed by taking 10%, 50% and 80% of the
 559 reported values. Since the model was giving an underestimation of expected dislocation
 560 densities, each study parameter was altered in such a way as to lead to their increase.
 561 Fig. 13 and Fig. 14 confirm that pipe diffusivity is the parameter with the highest influence
 562 on the model.

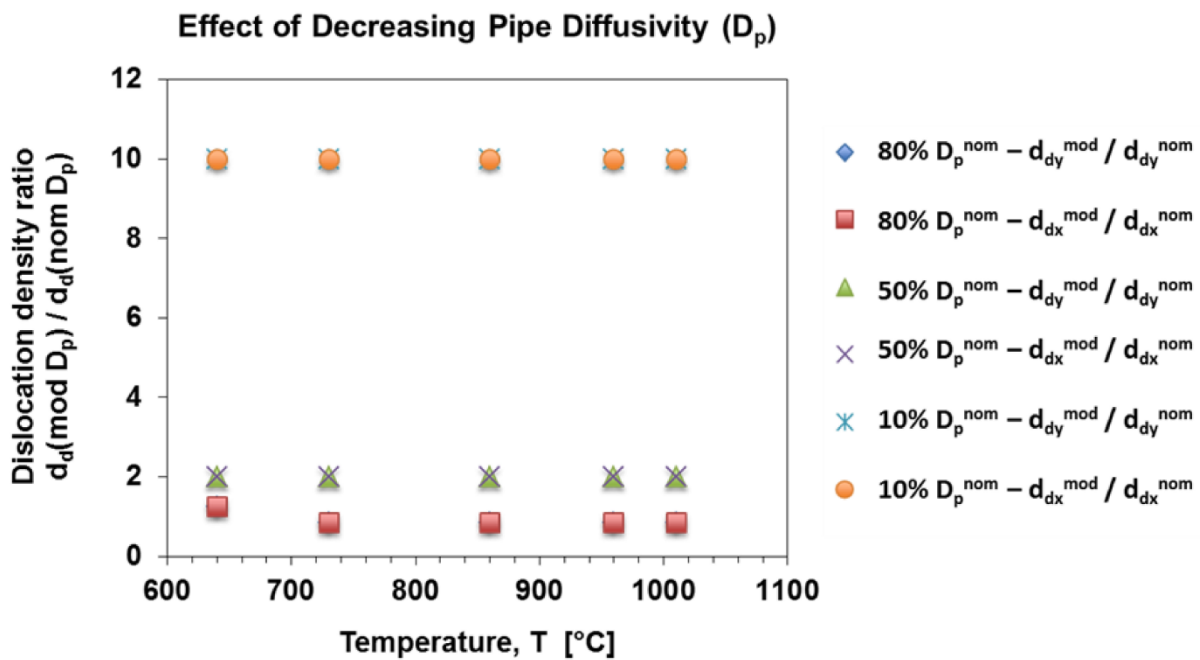


Fig. 13. Parametric study outcomes for varying pipe diffusion coefficient.

563

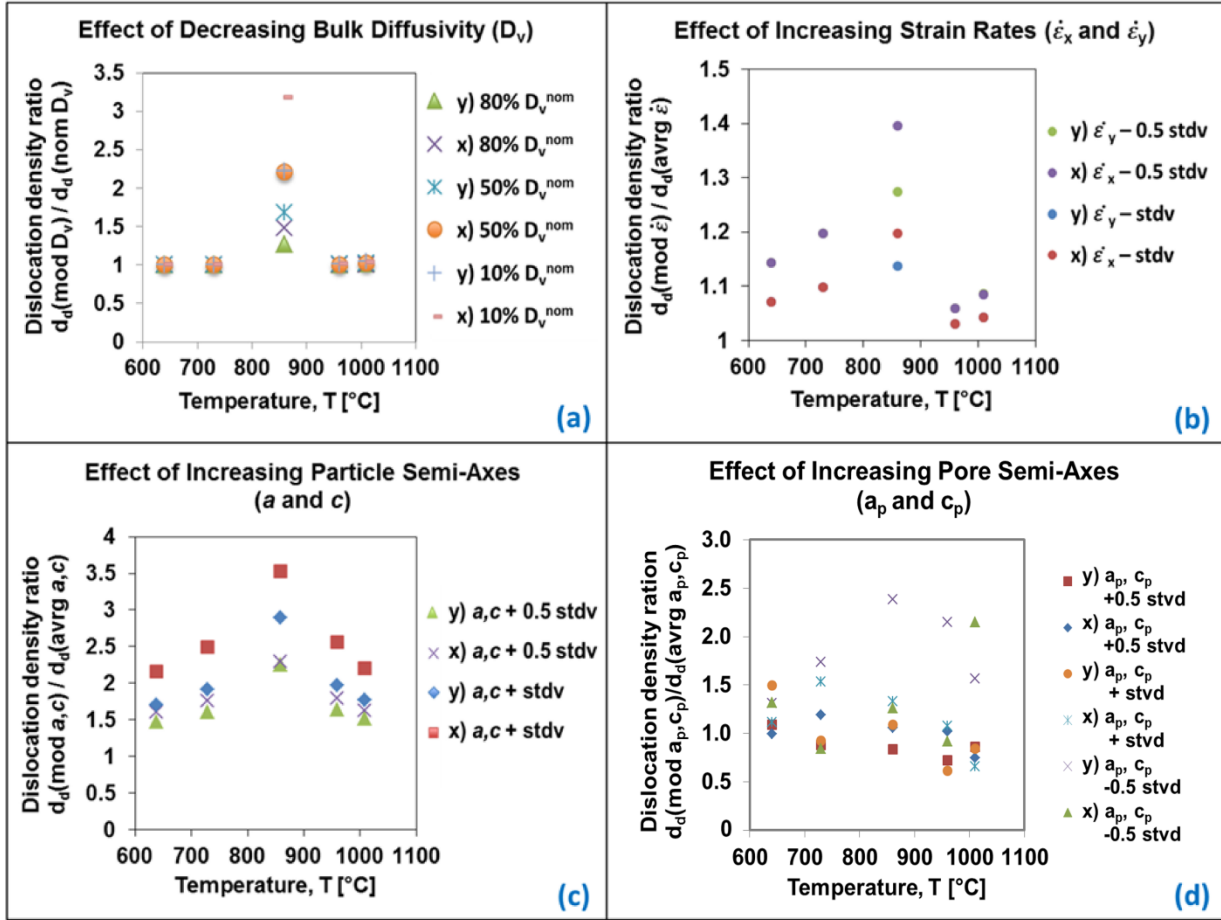


Fig. 14. Parametric study outcomes for varying (a) bulk diffusion coefficient; (b) strain rates; (c) particle semi-axes; (d) pore semi-axes.

564 In all Figures, the y-axis represents the ratio between dislocation density calculated with
 565 the modified parameter value (abbreviated as “mod”) and the one calculated with the
 566 original value (“nom” as for nominal for data from the literature and “avrg” as for average
 567 for experimental data). The legend specifies if we are referring to the x (transverse) or y
 568 (longitudinal) direction. It also provides the entity of the change in the considered
 569 parameter, namely the percentage of nominal value for the diffusivities and the addition
 570 or subtraction of the standard deviation (“stdv”, 50% or 100%) for strain rates and
 571 geometric features. The pipe diffusivity case is shown in Fig. 13, while Fig. 14 is for all
 572 other parameters.

573 A decrease in pipe diffusivity up to 10% of the value reported in the literature leads to an
574 increase in dislocation densities that reaches one order of magnitude. None of the other
575 parameters has such a significant effect, with a maximum factor of 3.5 reached in the
576 particle semi-axes study (noticeably, still at 860°C). Note how a variation in the value of
577 pipe diffusivity causes a change in calculated dislocation densities that is consistent for
578 all the temperatures considered (Fig. 13), while the other parameters (Fig. 14) present a
579 more unstable trend. The most striking case is the one relative to bulk diffusivity (part (a)
580 of Fig. 14), where, again at 860°C, we can observe a peak in the dislocation densities
581 ratio, in contrast with the other temperatures. This can be explained by looking at the bulk
582 diffusivity values and recalling how the parametric study procedure was set up. For data
583 extracted from the literature (diffusivities), we anticipated that various percentages of the
584 reported values were used. Since the bulk diffusivity reaches a maximum at 860°C, and
585 since its value at this temperature is orders of magnitude higher than at the other
586 temperatures considered in this study, its variation leads to a more significant oscillation
587 in the calculated dislocation densities. Such a trend is not as evident when considering
588 parameters that were measured experimentally, because here the standard deviation was
589 used as parameter variation range. It is, nevertheless, worth pointing out that the 860°C
590 samples were shown to be the most sensitive to the parametric variations in the majority
591 of cases. In part (b) of Fig. 14, only for 860°C it is possible to discern all the plotted data
592 points, while for the other temperatures they overlap.

593 A final verification of the model's sensitivity to the involved parameters was performed by
594 assessing the influence of the pores' curvature radii on the pipe diffusion coefficient. This
595 translates into checking the suitability of the method used to estimate the pores curvature

596 (shape approximated as ellipsoid) and verifying its effects on the mass transfer
597 mechanism. Our analysis shows that even much smaller values of pore radii (reduced of up to
598 more than one order of magnitude with respect to the initially measured ones) do not alter
599 significantly the pipe diffusivity values. This confirms the applicability of the ellipsoidal shape-
600 based approximation. An even higher accuracy can be achieved in the prosecution of this work
601 by evaluating the curvature of the pores via high resolution SEM visualization.

602 The uncertainty in pipe diffusivity data is thus confirmed to be the most likely cause of the
603 inaccuracy of the model at 860°C. In light of this finding, the literature data that had been
604 previously utilized were re-examined. In the work of Stechauner and Kozeschnik [90],
605 there are no experimental data available for temperatures above about 650°C. They
606 propose an extension of the curve until above 1400°C, most likely in analogy with the
607 grain boundary diffusivity data provided in the same plot, on which the data given in Table
608 3 are based. However, it is reasonable to assume that the slope of the curve for
609 dislocation pipe diffusivity as a function of temperature should decrease with increasing
610 temperatures, and not vice versa, as higher temperatures lead to a progressive
611 annihilation of the dislocations present in a material.

612 By back-calculating the values of pipe diffusivity based on our experimental data, a
613 modification to the Stechauner and Kozeschnik's fitting is proposed in Fig. 15.

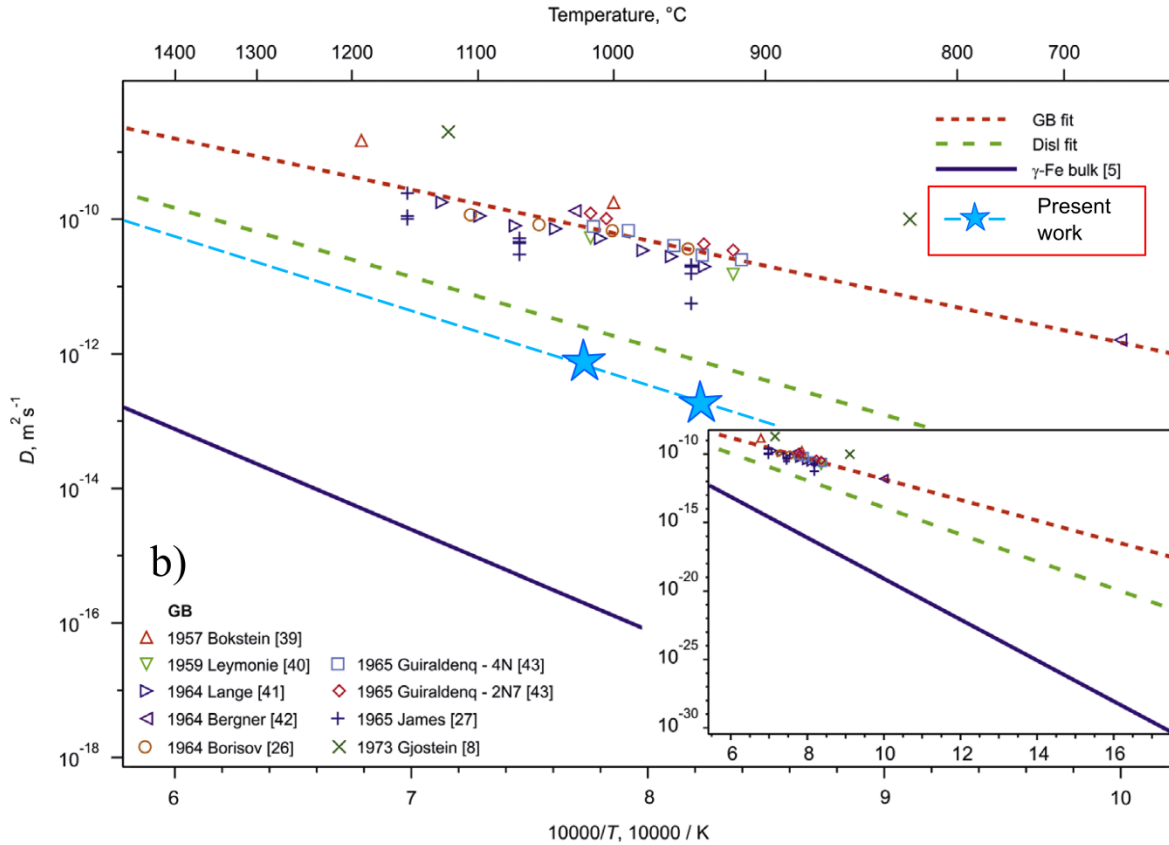
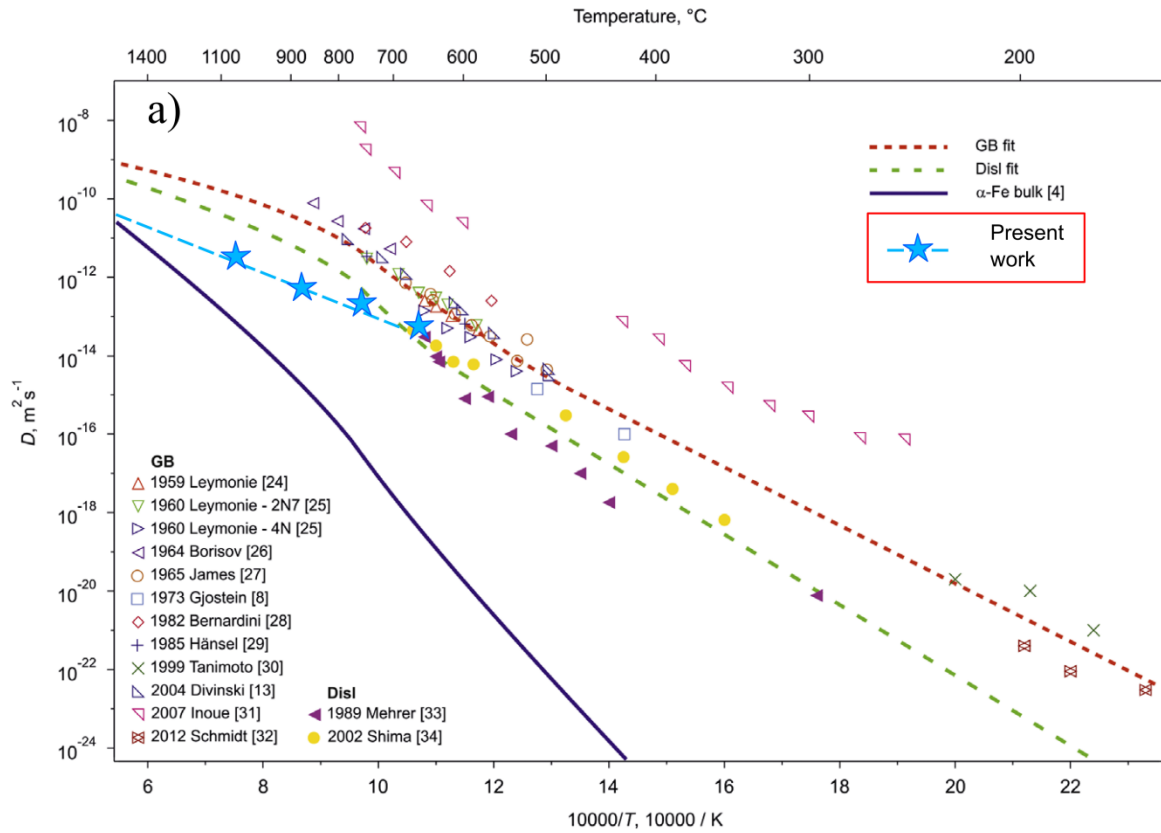


Fig. 155. Proposed modification of the dislocation pipe diffusivity fitting reported by Stechauner and Kozeschnik. a) α -Fe, b) γ -Fe, adapted from ref. [87].

614 The dislocation densities used for these back-calculations were the ones derived from the
615 nanoindentation measurements, since the overall amount is needed, including both
616 GNDs and SSDs. Fig. 15 is a reproduction of Fig. 2 from the original paper [87], with the
617 addition of the back-calculation outcomes (in bright blue). Specifically, the pipe
618 diffusivities resulted to be $6.01 \cdot 10^{-14} \text{ m}^2/\text{s}$ for 640°C , $1.53 \cdot 10^{-13} \text{ m}^2/\text{s}$ for 730°C , $3.20 \cdot 10^{-13}$
619 m^2/s for 860°C and $2.14 \cdot 10^{-12} \text{ m}^2/\text{s}$ for 960°C . Note that the pipe diffusivity at 640°C is in
620 very good agreement with the experimental data provided in the original paper, and that
621 the extrapolated curve approaches the bulk diffusivity one with increasing temperatures,
622 as expected with the progressive annealing of a cold-worked material. Note also that, at
623 the current state of this work, the distinction between edge and screw dislocations has
624 not been introduced. These two kinds of dislocations generally lead to different values of
625 pipe diffusivity. Such an investigation can be the object of future work.

626 The generally good agreement between the model and the experiments, together with
627 the subsequent parametric study, confirms the reliability and applicability of our
628 micromechanical model for the study of shrinkage anisotropy during sintering of cold-
629 pressed metallic powders.

630

631 **6. Conclusions**

632 The anisotropy of shrinkage during sintering of iron powders pre-compacted with a
633 uniaxial load is investigated. A micromechanical model is proposed for the shrinkage
634 rates along and perpendicular to the uniaxial load direction. Due to plastic deformation
635 introduced by the pre-sintering cold compaction, volume diffusion enhanced by

636 dislocation pipe diffusion is considered to be the dominant mass transfer mechanism
637 during post-cold-compaction sintering. The model parameters include the geometric
638 characteristics of the deformed porous structure, the structural defects (dislocations),
639 diffusivities and sintering temperatures. Dilatometric tests provide data on the shrinkage
640 rates, and image analysis is employed to quantify the characteristic dimensions of inter-
641 particle contacts and pores. Plugging these experimental results into this model,
642 dislocation densities are calculated at the inter-particle contacts in the longitudinal and
643 transverse directions. The applicability of the model is verified by comparing these
644 calculated values with dislocation densities estimated by means of nanoindentation and
645 EBSD techniques. Good agreement is found between experiments and our
646 micromechanical model, with the only exception of the temperature range between Curie
647 and austenitic points, in which the experimental value of dislocation pipe diffusion
648 coefficient is highly scattered. A parametric study confirms that pipe diffusivity is the
649 parameter that has the strongest influence on the model results, and offers the possibility
650 to back-calculate these pipe diffusivity values. As expected, higher dislocation densities
651 are found along the contacts perpendicular to the cold pressing direction, suggesting that
652 the pre-sintering cold compaction is the main cause for shrinkage anisotropy during
653 sintering.

654

655 **Acknowledgments**

656 DG, ET, EAO, and RKB acknowledge the support from the US National Science
657 Foundation Division of Civil and Mechanical Systems and Manufacturing Innovations for
658 this collaborative DMREF project (NSF Grant nos. CMMI 1234114 and CMMI 1502392).

659 The valuable support and cooperation of Prof. J. Taylor (Scripps Institution of
660 Oceanography, University of California, San Diego) and Prof. J. Torralba (Technical
661 University of Madrid, Spain) are gratefully acknowledged.

662

663 **References**

- 664 1. R.K. Bordia, Suk-Joong L. Kang and E.A. Olevsky, *Journal of the American Ceramic*
665 *Society* 2017, vol. 100, pp. 2314-2352.
- 666 2. J. Frenkel, *J. Phys.* (U. S. S. R) 1945, vol. 9, p. 385. 385–391.
- 667 3. B. Ya Pines, *J. Tech. Phys* 1946, vol. 16, p. 137.
- 668 4. G.C. Kuczynski, *Journal of Applied Physics* 1949, vol. 20, pp. 1160-1163.
- 669 5. J.K. Mackenzie and R Shuttleworth, *Proceedings of the Physical Society. Section B*
670 1949, vol. 62, p. 833.
- 671 6. C. Herring, *Journal of Applied Physics* 1950, vol. 21, pp. 301-303.
- 672 7. W.D. Kingery and Morris Berg, *Journal of Applied Physics* 1955, vol. 26, pp. 1205-
673 1212.
- 674 8. I.M. Lifshitz and Vitaly V Slyozov, *Journal of physics and chemistry of solids* 1961,
675 vol. 19, pp. 35-50.
- 676 9. R.L. Coble, *Journal of applied physics* 1961, vol. 32, pp. 787-792.
- 677 10. F. Thümmeler and W. Thomma, *Metallurgical Reviews* 1967, vol. 12, pp. 69-108.
- 678 11. D.L. Johnson, *Journal of Applied Physics* 1969, vol. 40, pp. 192-200.
- 679 12. H.E. Exner, *Rev. Powder Metall. Phys. Ceram.* 1,(1/4), 1979
- 680 13. F.B. Swinkels and MF Ashby, *Acta Metallurgica* 1981, vol. 29, pp. 259-281.

- 681 14. Schatt W., Friedrich E. (1987) Dislocation-Activated Sintering Processes. In:
682 Kuczynski G.C., Uskoković D.P., Palmour H., Ristić M.M. (eds) Sintering'85.
683 Springer, Boston, MA
- 684 15. Suk-Joong L. Kang: *Sintering: densification, grain growth and microstructure.*
685 *(Butterworth-Heinemann, 2004).*
- 686 16. M.N. Rahaman: *Sintering of ceramics.* (CRC press, 2007).
- 687 17. R.K. Bordia and GW Scherer, *Acta metallurgica* 1988, vol. 36, pp. 2393-2397.
- 688 18. R.K. Bordia and GW Scherer, *Acta Metallurgica* 1988, vol. 36, pp. 2399-2409.
- 689 19. R.K. Bordia and GW Scherer, *Acta Metallurgica* 1988, vol. 36, pp. 2411-2416.
- 690 20. E. A. Olevsky, *Mater Sci Eng R Rep* 1998, vol. 23, pp. 41-100.
- 691 21. E.A. Olevsky, V. Tikare and T. Garino, *Journal of the American Ceramic Society*
692 2006, vol. 89, pp. 1914-1922.
- 693 22. Z-Z Du and ACF Cocks, *Acta metallurgica et materialia* 1992, vol. 40, pp. 1969-1979.
- 694 23. RM McMeeking and LT Kuhn, *Acta metallurgica et materialia* 1992, vol. 40, pp. 961-
695 969.
- 696 24. H Riedel, H Zipse and J Svoboda, *Acta metallurgica et materialia* 1994, vol. 42, pp.
697 445-452.
- 698 25. D Bouvard and RM McMeeking, *Journal of the American Ceramic Society* 1996, vol.
699 79, pp. 666-672.
- 700 26. J. Pan: Computer modelling of sintering at different length scales. (Springer London,
701 2006).
- 702 27. HA Kuhn and CL Downey, *Int J Powder Met* 1971, vol. 7, pp. 15-25.
- 703 28. KT Kim and MM Carroll, *International journal of plasticity* 1987, vol. 3, pp. 63-73.

- 704 29. RJ Green, *International Journal of Mechanical Sciences* 1972, vol. 14, pp. 215-224.
- 705 30. Shima and M Oyane, *International Journal of Mechanical Sciences* 1976, vol. 18, pp.
706 285-291.
- 707 31. Arthur L Gurson, *Journal of engineering materials and technology* 1977, vol. 99, pp.
708 2-15.
- 709 32. Y Corapcioglu and T Uz, *Powder Technology* 1978, vol. 21, pp. 269-274.
- 710 33. MB Shtern, GG Serdyuk, LA Maximenko, YV Truhan and Yu M Shulyakov, *Naukova*
711 *Dumka*, Kiev 1982.
- 712 34. V. Tvergaard, *International Journal of fracture* 1982, vol. 18, pp. 237-252.
- 713 35. SM Doraivelu, HL Gegel, JS Gunasekera, JC Malas, JT Morgan and JF Thomas Jr,
714 *International Journal of Mechanical Sciences* 1984, vol. 26, pp. 527-535
- 715 36. N.A. Fleck, L.T. Kuhn and RM McMeeking, *Journal of the Mechanics and Physics of*
716 *Solids* 1992, vol. 40, pp. 1139-1162.
- 717 37. VV Skorokhod, *Dumka*, Kiev 1972.
- 718 38. D Giuntini, I-W Chen and EA Olevsky, *Scripta Materialia* 2016, vol. 124, pp. 38-41.
- 719 39. H.E. Exner and E.Arzt, In *Sintering Key Papers*, (Springer: 1990), pp 157-184.
- 720 40. A.L. Maximenko and Eugene A Olevsky, *Acta materialia* 2004, vol. 52, pp. 2953-
721 2963.
- 722 41. D. Giuntini, X. Wei, A.L. Maximenko, L. Wei, A.M. Ilyina and E.A. Olevsky,
723 *International Journal of Refractory Metals and Hard Materials* 2013, vol. 41, pp. 501-
724 506.
- 725 42. R.K. Bordia, R. Zuo, O. Guillon, S.M .Salamone and J. Rödel, *Acta materialia* 2006,
726 vol. 54, pp. 111-118.

- 727 43. H. Shang, A. Mohanram, E. Olevsky and R. K Bordia, *Journal of the European*
728 *Ceramic Society* 2016, vol. 36, pp. 2937-2945.
- 729 44. E.A. Olevsky, B. Kushnarev, A. Maximenko, V. Tikare and M. Braginsky,
730 *Philosophical Magazine* 2005, vol. 85, pp. 2123-2146.
- 731 45. F.Wakai and R.K. Bordia, *Journal of the American Ceramic Society* 2012, vol. 95,
732 pp. 2389-2397.
- 733 46. A. Zavaliangos, J.M. Missiaen and D. Bouvard, *Science of Sintering* 2006, vol. 38,
734 pp. 13-25
- 735 47. A. Zavaliangos and D. Bouvard, *International journal of powder metallurgy* 2000, vol.
736 36, pp. 58-65
- 737 48. A. Molinari, C. Menapace, E. Torresani, I. Cristofolini and M. Larsson, *Powder*
738 *Metallurgy* 2013, vol. 56, pp. 189-195..
- 739 49. A Molinari, E Torresani, C Menapace, I Cristofolini and M Larsson, In *Powdermet*
740 2013, (American Powder Metallurgy Institute: 2013), pp 525-532.
- 741 50. A Molinari and E Torresani, *Powder Metallurgy* 2015, vol. 58, pp. 323-327.
- 742 51. A. Molinari, I. Cristofolini, E. Torresani, *Adv. Powder Metall. Part. Mater.* (2015) 9–
743 18.
- 744 52. A. Molinari, E. Torresani, C. Menapace and M. Larsson, *Journal of the American*
745 *Ceramic Society* 2015, vol. 98, pp. 3431-3437.
- 746 53. W. Zhang and J.H. Schneibel, *Acta metallurgica et materialia* 1995, vol. 43, pp. 4377-
747 4386.
- 748 54. EW Hart, *Acta Metallurgica* 1957, vol. 5, p. 597
- 749 55. M.Cohen, *Transactions of the Japan Institute of Metals* 1970, vol. 11, pp. 145-151

- 750 56. E. Olevsky and V. Skorohod, *Le Journal de Physique IV* 1993, vol. 3, pp. C7-739-
751 C7-742.
- 752 57. P.M. Raj and W.R. Cannon, *Journal of the American Ceramic Society* 1999, vol. 82,
753 pp. 2619-2625..
- 754 58. P.M.Raj, A. Odulena and W.R. Cannon, *Acta materialia* 2002, vol. 50, pp. 2559-
755 2570..
- 756 59. S Krug, JRG Evans and JHH Ter Maat, *Journal of the European Ceramic Society*
757 2002, vol. 22, pp. 173-181.
- 758 60. E Torresani, G Ischia and A Molinari, In *European Congress and Exhibition on*
759 *Powder Metallurgy. European PM Conference Proceedings*, (The European Powder
760 Metallurgy Association: 2014), p 1
- 761 61. W.D. Nix and H. Gao, *Journal of the Mechanics and Physics of Solids* 1998, vol. 46,
762 pp. 411-425.
- 763 62. J.G. Swadener, E.P. George and G.M. Pharr, *Journal of the Mechanics and Physics*
764 *of Solids* 2002, vol. 50, pp. 681-694.
- 765 63. Z Zong, J Lou, OO Adewoye, AA Elmustafa, F Hammad and WO Soboyejo, *Materials*
766 *Science and Engineering: A* 2006, vol. 434, pp. 178-187.
- 767 64. M. Gee, K. Mingard and B. Roebuck, *International Journal of Refractory Metals and*
768 *Hard Materials* 2009, vol. 27, pp. 300-312.
- 769 65. DP Field, CC Merriman, N Allain-Bonasso and F Wagner, *Modelling and Simulation*
770 *in Materials Science and Engineering* 2012, vol. 20, p. 024007.
- 771 66. C. Zhu, T. Harrington, V.a Livescu, G.T. Gray and K.S. Vecchio, *Acta Materialia*
772 2016, vol. 118, pp. 383-394.

- 773 67. Y. Shima, Y. Ishikawa, H. Nitta, Y. Yamazaki, K.Mimura, M. Isshiki and Y.Iijima,
774 *Materials Transactions* 2002, vol. 43, pp. 173-177.
- 775 68. A Verma, M Sundararaman, JB Singh and SA Nalawade, *Measurement Science and*
776 *Technology* 2010, vol. 21, p. 105106
- 777 69. J. Park, M. Jung and Y-K Lee, *Journal of Magnetism and Magnetic Materials* 2015,
778 vol. 377, pp. 193-196.
- 779 70. E. D. Hondros and N. P. Allen, *Proc. R. Soc. Lond. A* 1965 286 (1407), pp.479-
780 498.71. G.M. Pharr, E.G. Herbert and Y. Gao, *Annual Review of Materials Research*
781 2010, vol. 40, pp. 271-292.
- 782 72. H. Gao and Y. Huang, *International Journal of Solids and Structures* 2001, vol. 38,
783 pp. 2615-2637.
- 784 73. G.Z. Voyiadjis and A.H. Almasri, *Journal of engineering mechanics* 2009, vol. 135,
785 pp. 139-148.
- 786 74. D. Faghihi and G.Z. Voyiadjis, *Mechanics of Materials* 2012, vol. 44, pp. 189-211.
- 787 75. JF Nye, *Acta metallurgica* 1953, vol. 1, pp. 153-162.
- 788 76. E. Kröner, *Continuum Theory of Dislocation and Self-Stresses*, Springer, 1958.
- 789 77. C.Zhu, V. Livescu, T. Harrington, O. Diplo, G.T. Gray and K.S. Vecchio,
790 *International Journal of Plasticity* 2017, vol. 92, pp. 148-163
- 791 78. E. Demir, D. Raabe, N. Zaafarani and S. Zaefferer, *Acta Materialia* 2009, vol. 57, pp.
792 559-569.
- 793 79. BC Larson, Wenge Yang, JZ Tischler, GE Ice, JD Budai, W Liu and H Weiland,
794 *International Journal of Plasticity* 2004, vol. 20, pp. 543-560.

- 795 80. Angus J Wilkinson and David Randman, *Philosophical magazine* 2010, vol. 90, pp.
796 1159-1177.
- 797 81. FRD Boer, R Boom, W Mattens, A Miedema and A Niessen, (North Holland,
798 Amsterdam: 1989).
- 799 82. WR Tyson and WA Miller, *Surface Science* 1977, vol. 62, pp. 267-276.
- 800 83. TA Roth, *Materials Science and Engineering* 1975, vol. 18, pp. 183-192.
- 801 84. A Inoue, H Nitta and Y Iijima, *Acta Materialia* 2007, vol. 55, pp. 5910-5916.
- 802 85. R.E. Smallman and A.H.W. Ngan: *Physical metallurgy and advanced materials*.
803 (Butterworth-Heinemann, 2011).
- 804 86. W.F. Gale and T.C. Totemeier: *Smithells metals reference book*. (Elsevier, 2003).
- 805 87. G Stechauner and E Kozeschnik, *Calphad* 2014, vol. 47, pp. 92-99.
- 806 88. Nosewicz S, Rojek J, Chmielewski M. Pietrzak K, *Advanced Powder Technology*,
807 Vol. 28, 2017, 1745-1759

808

809 **Figure Captions**

810 **Fig.1.** Schematics of the study domain representative of the porous material's structure:
811 (a) 3-D representation, where δ is the inter-particle boundary thickness; (b) 2-D view with
812 micromechanics parameters designation.

813 **Fig.2.** Dilatometry samples for the longitudinal (y, in red) and transverse (x, in blue)
814 shrinkage rates analysis, as derived from cold-pressed Charpy bars. The direction of
815 uniaxial compaction is marked.

816 **Fig.3.** Example of dilatometric curve for sintering with holding at 960°C: (a) temperature
817 regime and shrinkages in the longitudinal (y) and transverse (x) direction for the entire
818 processing route; (b) shrinkage curves during the isothermal holding time.

819 **Fig.4.** Individuation of inter-particle contacts length (L) and inclination (λ) from image
820 analysis of SEM micrographs.

821 **Fig.5.** Individuation of the pores' geometrical parameters from image analysis of SEM
822 micrographs.

823 **Fig.6.** Examples of micrographs of nanoindentation tests: (a) with 55 mN load on a
824 sample sintered at 640°C (for a longitudinal contact); (b) with a 95 mN load on a sample
825 sintered at 960°C (for a transverse contact). In the latter case the two involved powder
826 particles have been highlighted.

827 **Fig.7.** Example of EBSD results for GND density distribution (measured as \log_{10} of GNDs
828 per m^2) and average disorientation angle distribution: (a) GND density distribution for a
829 sample sintered at 1010°C, acquired at 2000X and with 200 nm step size, with selection
830 of boxes around representative x and y inter-particle contacts; (b) GND density along y
831 and (d) along x; (c) average disorientation angle distribution around an inter-particle
832 boundary along y and (e) along x.

833 **Fig.8.** Steps followed for the EBSD analysis of a sample sintered at 1010°C: (a) pattern
834 quality image showing the individuation of longitudinal and transverse particle boundaries
835 based on pores at triple junctions; (b) EBSD scan of the pre-selected regions; (c) GND
836 density map around the particle boundaries; (d) particle boundary selection refinement
837 with an $8 \times 4 \mu m$ box.

838 **Fig.9.** Example of derivation of isothermal shrinkage rate in the transverse direction,
839 $\dot{\epsilon}_x(t)$, for a sample sintered at 960°C. (a) Dilatometric curve with isothermal part
840 highlighted between dashed lines; (b) corresponding isothermal shrinkage rate.

841 **Fig.10.** Inter-particle contact lengths a and c at the various sintering temperatures.

842 **Fig.11.** Pores semi-axes lengths, a_p and c_p , at the different temperatures (a) values
843 obtained from image analyses; (b) average values \bar{a}_p and \bar{c}_p .

844 **Fig.12.** Dislocation density values: (a) comparison between experimental and modeling
845 results; (b) ratio between experimental and modeling results.

846 **Fig.13.** Parametric study outcomes for varying pipe diffusion coefficient.

847 **Fig.14.** Parametric study outcomes for varying (a) bulk diffusion coefficient; (b) strain
848 rates; (c) particle semi-axes; (d) pore semi-axes.

849 **Fig.15.** Proposed modification of the dislocation pipe diffusivity fitting reported by
850 Stechauner and Kozeschnik. a) α -Fe, b) γ -Fe, adapted from ref. [90].

851
852

853

854

855

TABLES

856 **Tab.1.** Shrinkage rates along x (transverse) and y (longitudinal) directions at the different
857 sintering temperatures.

T [°C]	$\dot{\epsilon}_x$ [1/s]	$\dot{\epsilon}_y$ [1/s]
640	$-4.04 \cdot 10^{-5}$	$-5.31 \cdot 10^{-5}$
730	$-8.68 \cdot 10^{-5}$	$-1.65 \cdot 10^{-4}$
860	$-8.41 \cdot 10^{-5}$	$-1.23 \cdot 10^{-4}$
960	$-3.74 \cdot 10^{-5}$	$-3.54 \cdot 10^{-5}$
1010	$-4.42 \cdot 10^{-5}$	$-4.54 \cdot 10^{-5}$

858

859

860

861

862 **Tab.2.** Nanoindentation hardness (H) and indentation depth (h) values measured by
 863 nanoindentation at the inter-particle contact areas. F indicates the load applied during the
 864 indentation test.

Specimens sintered at 640°C									
	Contacts along y				Contacts along x				
F [mN]	H [GPa]		h [μm]		H [GPa]		h [μm]		
	mean	st.dev	mean	st.dev	mean	st.dev	mean	st.dev	
55	5.02	2.27	0.58	0.13	5.07	4.31	0.69	0.30	
75	4.92	1.22	0.67	0.09	5.06	0.27	0.64	0.04	
95	4.89	1.89	0.69	0.22	4.95	3.15	0.80	0.26	
Specimens sintered at 730°C									
	Contacts along y				Contacts along x				
F [mN]	H [GPa]		h [μm]		H [GPa]		h [μm]		
	mean	st.dev	mean	st.dev	mean	st.dev	mean	st.dev	
55	4.20	1.70	0.70	0.18	4.47	1.43	0.66	0.12	
75	4.17	0.58	0.76	0.05	4.46	0.49	0.72	0.02	
95	4.12	0.80	0.83	0.12	4.39	1.20	0.78	0.16	
Specimens sintered at 860°C									
	Contacts along y				Contacts along x				
F [mN]	H [GPa]		h [μm]		H [GPa]		h [μm]		
	mean	st.dev	mean	st.dev	mean	st.dev	mean	st.dev	
55	4.28	1.95	0.68	0.20	3.45	1.22	0.77	0.17	

75	4.09	1.91	0.78	0.18	3.42	1.01	0.81	0.18
95	4.09	1.23	0.83	0.18	3.36	0.49	0.90	0.11
Specimens sintered at 960°C								
	Contacts along y				Contacts along x			
	H [GPa]		h [μm]		H [GPa]		h [μm]	
F [mN]	mean	st.dev	mean	st.dev	mean	st.dev	mean	st.dev
55	3.40	0.47	0.76	0.06	3.35	0.83	0.79	0.12
75	3.14	1.12	0.97	0.07	3.16	1.34	0.91	0.17
95	2.97	0.52	1.00	0.11	3.10	1.54	1.03	0.24

865

866 **Tab.3.** Volume and pipe diffusivities at equilibrium. The pipe diffusion coefficient is
867 calculated by plugging D_0 and Q in an Arrhenius-type relation. D_0 and Q change values
868 depending on the iron phase. T_a is the room temperature and T_m is the melting point.

D_v		D_p				
T [°C]	[m²/s]	T [°C]	Q[kJ/mol]	D₀ [m²/s]	T [°C]	D_p [m²/s]
640	$1.09 \cdot 10^{-19}$	T_a-420	200	$4.50 \cdot 10^{-3}$	640	$1.63 \cdot 10^{-14}$
730	$6.99 \cdot 10^{-18}$	420-769	200	$4.50 \cdot 10^{-3}$	730	$1.74 \cdot 10^{-13}$
860	$7.77 \cdot 10^{-16}$	769-910	200	$4.50 \cdot 10^{-3}$	860	$2.72 \cdot 10^{-12}$
960	$2.71 \cdot 10^{-17}$	911-T_m	185	$4.50 \cdot 10^{-5}$	960	$6.56 \cdot 10^{-13}$
1010	$8.85 \cdot 10^{-17}$	911-T_m	185	$4.50 \cdot 10^{-5}$	1010	$1.33 \cdot 10^{-12}$

869
870

871 **Tab.4.** Dislocation densities for transverse contacts (d_{dx}) and for longitudinal contacts
 872 (d_{dy}).

Temperature, T [°C]	Nanoindentation		EBSD		Model	
	d_y [1/m ²]	d_x [1/m ²]	d_y [1/m ²]	d_x [1/m ²]	d_y [1/m ²]	d_x [1/m ²]
640	$8.26 \cdot 10^{15}$	$1.17 \cdot 10^{16}$	$1.02 \cdot 10^{15}$	$1.04 \cdot 10^{15}$	$2.21 \cdot 10^{16}$	$2.08 \cdot 10^{16}$
730	$1.06 \cdot 10^{16}$	$1.20 \cdot 10^{16}$	$1.02 \cdot 10^{15}$	$1.06 \cdot 10^{15}$	$7.00 \cdot 10^{15}$	$7.43 \cdot 10^{15}$
860	$2.98 \cdot 10^{15}$	$4.98 \cdot 10^{15}$	$8.61 \cdot 10^{14}$	$8.88 \cdot 10^{14}$	$4.28 \cdot 10^{14}$	$4.85 \cdot 10^{14}$
960	$6.12 \cdot 10^{14}$	$1.78 \cdot 10^{15}$	--	--	$2.34 \cdot 10^{15}$	$2.60 \cdot 10^{15}$
1010	--	--	$8.41 \cdot 10^{14}$	$9.29 \cdot 10^{14}$	$1.72 \cdot 10^{15}$	$2.13 \cdot 10^{15}$

873